

Subglacial Canal Initiation Driven by Till Erosion

Indraneel Kasmalkar¹, Elisa Mantelli¹, and Jenny Suckale¹

¹Stanford University

November 22, 2022

Abstract

The distribution and drainage of meltwater at the base of glaciers sensitively affects fast ice flow. Classical studies suggest that thin meltwater films between the overlying ice and a hard-rock bed channelize into efficient drainage elements by melting the overlying ice. However, these studies do not account for the presence of soft deformable sediment observed underneath many West Antarctic ice streams, and the inextricable coupling that sediment exhibits with meltwater drainage. Our work presents an alternate channel initiation mechanism where meltwater films grow by eroding the sediment beneath. We conduct a linearized stability analysis on a meltwater film flowing over an erodible bed. We solve the Navier Stokes equations for the film flow, and we compute bed evolution with the Exner equation. We identify a regime where the coupled dynamics of hydrology and sediment transport generate a morphological instability that would indicate channel initiation. We show that this instability operates at time scales much faster than ice dynamics, thus occurring prior to the classical channelization instabilities. We discuss the physics of the instability using the framework of ripple formation on erodible beds.

Subglacial Canal Initiation Driven by Till Erosion

I. Kasmalkar¹, E. Mantelli², and J. Suckale²

May 1, 2019

Abstract

The distribution and drainage of meltwater at the base of glaciers sensitively affects fast ice flow. Classical studies suggest that thin meltwater films between the overlying ice and a hard-rock bed channelize into efficient drainage elements by melting the overlying ice. However, these studies do not account for the presence of soft deformable sediment observed underneath many West Antarctic ice streams, and the inextricable coupling that sediment exhibits with meltwater drainage. Our work presents an alternate channel initiation mechanism where meltwater films grow by eroding the sediment beneath. We conduct a linearized stability analysis on a meltwater film flowing over an erodible bed. We solve the Navier Stokes equations for the film flow, and we compute bed evolution with the Exner equation. We identify a regime where the coupled dynamics of hydrology and sediment transport generate a morphological instability that would indicate channel initiation. We show that this instability operates at time scales much faster than ice dynamics, thus occurring prior to the classical channelization instabilities. We discuss the physics of the instability using the framework of ripple formation on erodible beds.

1 Introduction

Liquid water is present underneath more than half of the Antarctic Ice Sheet [56]. The hydrological environments in which this water is stored and transported are diverse, ranging from subglacial lakes to water-saturated wetlands situated underneath fast flowing ice [58]. Out of these, the drainage system underneath ice streams, corridors of rapid ice flow that are tens of kilometers thick and hundreds of kilometers long, is not only the most spatially extensive but also inextricably coupled with the dynamics of the overlying ice flow [6, 44, 57, 23]. While our understanding of this subglacial water drainage system is incomplete, it is becoming increasingly clear that it is both spatially and temporally variable [24].

Water flow, however, is not the only dynamic component in the extensive wetlands underneath the West Antarctic ice streams. Large portions of this area rest on weak and unconsolidated sediment, commonly referred to as till [25]. Samples collected from the subglacial environment at Ice Stream B, Siple

Coast, have revealed a fine-grained, clay-rich lithology [68] that likely experiences significant deformation [1, 38, 66] and transport [1] due to streaming ice flow.

The insight that sediments play an important role in subglacial hydrology and ice flow is not new, and several previous models of subglacial hydrology have made progress in that regard. Early attempts treated the subglacial horizon as an aquifer with porous flow being the primary means of water drainage [65, 46]. While percolation of water into the till is clearly important in altering the basal resistance that the till layer provides to ice flow [69, 7], water transport through the till layer is likely very inefficient [2] because of the low permeability of clay-rich till [37, 38]. Therefore, later models have replaced the idea of Darcian-type water transport through a porous aquifer by the assumption that the majority of water flows in a thin pressurized film between the ice and the till [74, 2, 45, 43].

Walder [72] identified a problem with large-scale water transport via film flow, namely that meltwater films over hard beds are fundamentally unstable. His work [72] highlights that a small perturbation in film thickness would lead to higher flow speed, which would induce greater viscous dissipation and preferential carving into the overlying ice. Creyts and Schoof [14] later showed that this instability is partially suppressed by bed roughness, reinvigorating the idea that films could support meltwater transport at least up to a certain thickness. They argue that stress localization on bed protrusions leads to enhanced ice roof closure that counters film expansion, thus entailing the possibility of finite-sized films. Nonetheless, as the thickness of the meltwater film grows, the water would eventually carve into the ice, thus transforming the film into a more efficient drainage element such as a R othlisberger channel [60] or linked cavities [27]. This insight is reflected in current subglacial hydrology models for hard beds that generally include both films and channels [61, 62, 35, 34, 76].

In hard bed settings, efficient drainage systems will be inevitably carved into the ice [27]. But the wide-spread occurrence of till under ice sheets [67, 68] suggests the possibility of drainage elements incised into the sediment layer, commonly referred to as canals [73, 52, 53, 41, 16]. Walder and Fowler [73] show that dynamic till, in particular the processes of till erosion and deformation, is key to the sustenance of canals. Ng [52] builds on the work by Walder and Fowler by describing the meltwater flux and sediment transport dynamics over the longitudinal span of a canal. Since the coupled processes of meltwater and till feature prominently in the functioning of canals, it is likely that they also play a key role in the formation of canals. Departing from the classical idea of Walder’s instability [72] that films grow into channels by melting the ice above, we hypothesize that meltwater films on soft beds grow into canals by eroding the sediment beneath.

Kyrke-Smith and Fowler [43] have previously studied that evolution of meltwater films on soft beds. They emphasize the role of dynamic till by explicitly including erosion and deformation into their model. However, they retain the assumption from the hard-bed setting that bed roughness stabilizes thin films [14]. This assumption implicitly imposes key dynamics involving ice, water and till onto the soft-bed setting without resolving the underlying processes. Our

work provides an alternative framework for the stability of meltwater films that relies purely on the coupled dynamics of hydrology and sediment transport.

We model the meltwater film as flow over an erodible bed and study potential channelization via morphological instabilities, similar to granular ripple formation, e.g., [39, 29, 59, 11]. We compute bed-form evolution using the classical Exner equation which represents sediment mass conservation. We use the 3-D Navier-Stokes equations to compute flow velocities within the film. A depth-averaged velocity approach, while commonly used for meltwater films [27], is not suitable for morphological instabilities because of the lack of resolution of near-bed flow dynamics [13, 47].

Walder’s instability of film expansion via dissipation-induced melting of the ice is known to drive channel initiation [72, 74]. To identify potential instabilities that may occur prior to Walder’s instability, we assume non-turbulent flow within our meltwater film. This assumption allows us to study the film within a regime where dissipation and associated ice melt is mitigated. In this regime, and over length scales comparable to film thickness, the overlying ice is effectively decoupled from the film hydrology. Our setup then allows us to explore instabilities associated with the sediment bed rather than the ice.

We conduct a linearized stability analysis to identify the mechanisms within the meltwater film system that lead to instabilities. Our findings point to advection within the film flow as a key destabilizer of the system, which is consistent with previous studies of ripple formation instabilities [39, 40]. On the other hand, prior studies generally attribute the stability of films with regard to short-wavelength perturbations to diffusive mechanisms within the sediment transport dynamics [11]. Our work identifies a hydrodynamic mechanism based on flow acceleration that can stabilize the film at short wavelengths. While sediment-based mechanisms may provide additional stability to the system, our work shows that they are not necessary for the selection of the fastest growing perturbation wavelength.

2 Model

We consider a thin layer of subglacial meltwater, flowing between two initially homogeneous, infinitely extended layers of ice and till on the top and bottom, respectively, both inclined at an angle β with respect to the horizontal. The surface of the ice possesses its own slope, α with respect to its base. We adopt a Cartesian coordinate system (x, y, z) . As shown in Figure 1, the x -axis is parallel to the bed and denotes the along-flow direction, while the y - and z -axes span the cross-flow direction and the depth of the film. We represent the ice-water interface by $z = h(x, y, t)$ and the till-water interface by $z = r(x, y, t)$.

Our model includes two components: fluid flow, described by mass and momentum conservation; and sediment transport, which governs the evolution of the till-water interface. We discuss the thermal and mechanical interactions of ice and water, and revisit the underlying assumptions in Section 4. The key thermal interaction between ice and water lies in the energy budget at the

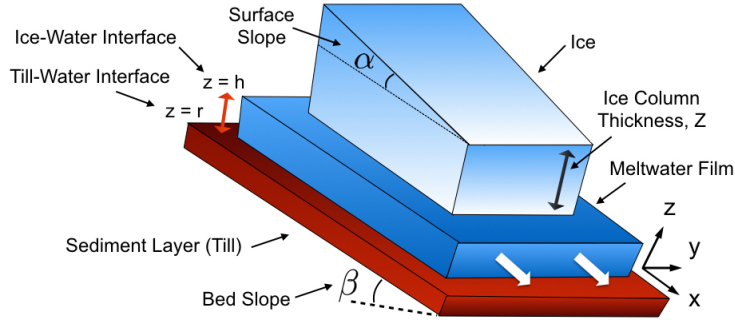


Figure 1: Setup of the model. The thicknesses of the three layers is not drawn to scale. The ice column is several orders of magnitude thicker than the meltwater film.

corresponding interface, namely the melting of the ice caused by the heat flux from the film. We assume a non-turbulent flow regime where the dissipation-induced melting of the ice is suppressed. Combined with the assumption that sediment transport processes are significantly faster than ice-related processes, we can effectively treat the ice-water interface as a fixed boundary. The key mechanical interaction between ice and water is the pressure exerted on the film by the weight of the overlying ice column. The corresponding pressure gradient serves as a driving force for the film flow.

We now present the governing equations of the meltwater film system.

2.1 Hydrology

Conservation of mass within the subglacial meltwater film, along with incompressibility, yields,

$$\nabla \cdot \mathbf{u} = 0, \quad \text{on } r < z < h, \quad (1)$$

where $\mathbf{u} = (u, v, w)$ is the fluid velocity along the axes (x, y, z) respectively.

The Navier-Stokes equations express momentum conservation within the meltwater film,

$$\frac{\partial \mathbf{u}}{\partial t} + \mathbf{u} \cdot \nabla \mathbf{u} = -\frac{1}{\rho} \nabla p + \nu \nabla^2 \mathbf{u} + \mathbf{g}, \quad \text{on } r < z < h, \quad (2)$$

where t stands for time, ν is the kinematic viscosity of water at the melting point and ρ is the density of water, p is the fluid pressure, $\mathbf{g} = (g \sin \beta, 0 - g \cos \beta)$ is the gravitational force, and g is the gravitational acceleration on the Earth's surface.

We assume that the ice-water interface is a fixed boundary and apply the no-slip condition,

$$u = 0, \quad v = 0, \quad w = 0, \quad \text{at } z = h. \quad (3)$$

The overlying ice affects the pressure in the film through its overburden weight. The balance of normal stresses of the ice and water at the interface is given by,

$$p = p_a + (Z_0 + Z_1(x))\rho_i g \cos \beta, \quad \text{at } z = h, \quad (4)$$

where p_a is the atmospheric pressure at the surface of the ice and ρ_i is the density of ice. The term Z_0 is the leading order ice thickness measured perpendicular to the bed. At length scales comparable to meltwater film thickness, Z_0 is constant, indicating that the ice surface is parallel to the bed. The term $Z_1(x)$ represents smaller scale change in the ice thickness along x . In (4), the fluid normal stress at the ice-water interface reduces to the pressure p as a consequence of (1) and (3). We approximate the normal stress imposed by the ice on the film by weight of the overlying ice column. This approximation follows from the Shallow Ice assumption, namely that the ice thickness is considerably smaller than the ice sheet length scale.

The till-water interface is also a solid boundary where the no slip condition would apply. Since the bed is erodible, the vertical velocity satisfies the kinematic boundary condition,

$$u = 0, \quad v = 0, \quad w = \frac{\partial r}{\partial t}, \quad \text{at } z = r. \quad (5)$$

2.2 Sediment Bed-load Transport

We model the evolution of the till-water interface $z = r(x, y, t)$ through the Exner equation,

$$\frac{\partial r}{\partial t} + \frac{1}{1 - \phi_m} \nabla \cdot \mathbf{q} = 0 \quad (6)$$

where ϕ_m is the mean sediment porosity and $\mathbf{q} = (q_x, q_y)$ is the sediment flux vector. The Exner equation is a mass conservation statement for the sediment layer, stating that the till-water interface evolves in time according to gradients of the sediment flux.

To close the model, we use a classical constitutive relation that expresses the sediment flux \mathbf{q} as a function of the shear stress applied by the water film onto the bed [50, 77, 70],

$$\mathbf{q} = \hat{\boldsymbol{\tau}} F \left(\frac{|\boldsymbol{\tau}|}{(\rho_s - \rho)gD} \right) D \sqrt{\frac{\rho_s - \rho}{\rho}} gD, \quad (7)$$

where D is the sediment grain diameter, ρ_s is the sediment density and F is a non-dimensional function to be defined later. The bed stress vector, $\boldsymbol{\tau} = (\tau_x, \tau_y)$, and its unit vector, $\hat{\boldsymbol{\tau}}$, are given by,

$$\boldsymbol{\tau}_i = \rho \nu \mathbf{t}_i^T (\nabla \mathbf{u} + \nabla \mathbf{u}^T) \mathbf{n}, \quad \hat{\boldsymbol{\tau}} = \frac{\boldsymbol{\tau}}{|\boldsymbol{\tau}|}, \quad \text{at } z = r. \quad (8)$$

The vectors \mathbf{t}_x and \mathbf{t}_y are the unit tangent vectors to the bed in the x - and y - directions respectively, and \mathbf{n} is the normal surface vector for the bed $z = r(x, y, t)$.

There is considerable disagreement functional form of the relationship between sediment flux and bed shear stress, e.g., [64, 22, 31]. As a result, there is a variety of empirically derived power-law formulas in the literature, each calibrated to its own setting, e.g., [77, 70]. This diversity of forms highlights that the physics of bed-load transport is not yet fully understood.

Observations of bed-load transport highlight that there is a threshold value of bed stress below which there is purportedly no grain motion at the bed, as discussed in the classical work by Shields [64] and others, for example [51, 10, 36]. Housais et. al. [36] suggest that this threshold value, known as the critical Shields stress, marks a phase transition for the granular material. Below the threshold the bed stress is balanced by extremely slow creep deep in the sediment, while exceeding the threshold leads to the formation of an overlying bed-load layer undergoing dense granular flow at a time-scale comparable to that of near-bed fluid flow. Experimental studies [36, 10, 55] characterize this phase transition as a toggle point, where bed-load transport is deemed active only when the fluid bed stress exceeds the threshold stress. Our model utilizes the threshold in the same manner and we assume that the film bed stress always exceeds this threshold. This assumption is a key prerequisite for the linearization stability analysis conducted in Section 5.

For the purposes of this study, we choose the classic functional by Meyer-Peter and Müller [50],

$$F \left(\frac{|\boldsymbol{\tau}|}{[\boldsymbol{\tau}_b]} \right) = A \left(\frac{|\boldsymbol{\tau}|}{[\boldsymbol{\tau}_b]} - \tau_c^* \right)^m, \quad A = 8, \quad m = 1.5, \quad (9)$$

where τ_c^* is the non-dimensional critical Shields stress, and $[\boldsymbol{\tau}_b] = (\rho_s - \rho)gD$ is the bed stress scale as per the functional [50]. We do not include sediment suspension in our model since the lack of turbulence precludes the possibility of sediment saltation, e.g., [4, 28, 10].

We choose a specific functional for the purposes of our analysis, but our approach can be repeated with any other functional satisfying (7). The linear stability analysis conducted in Section 5 demonstrates that, as long as the form expressed in (7) holds, the exact choice of functional does not alter the overall stability of the meltwater film. Insensitivity to the functional broadens the applicability of our model to a wide variety of glaciological settings.

2.3 Steady State

We solve the system of equations (1-6) for the steady state. We assume that the steady state solution is uniform in the x and y directions.

The ice topography imposes a driving force on the fluid, as described in (4). The flow pressure gradient arises from the small-scale change in ice thickness, $\frac{\partial Z_1}{\partial x}$. We parametrize this term as,

$$\frac{\partial Z_1}{\partial x} = -\tan \alpha, \quad (10)$$

where α is a constant that can be considered as the angle of the ice surface with respect to the bed. We combine both the driving forces, gravity (2) and ice overburden (4), into a single parameter,

$$\Pi = \sigma_i \tan \alpha \cos \beta + \sin \beta, \quad \text{where} \quad \sigma_i = \frac{\rho_i}{\rho}. \quad (11)$$

We denote steady state variables by an overlying bar. We define H as half the steady state film thickness. The constant of half allows us to avoid re-scaling in other equations.

$$\bar{h}(x, y) = 2H, \quad \bar{r}(x, y) = 0, \quad (12)$$

$$\bar{u}(x, y, z) = \frac{H^2 g \Pi}{2\nu} \frac{z}{H} \left(2 - \frac{z}{H}\right), \quad \bar{v} = 0, \quad \bar{w} = 0, \quad \text{on} \quad \bar{r} \leq z \leq \bar{h}, \quad (13)$$

$$\bar{p}(x, y, z) = p_a + \rho_i g Z_0 \cos \beta - \rho g x \tan \alpha \cos \beta, \quad \text{on} \quad \bar{r} \leq z \leq \bar{h}, \quad (14)$$

$$\bar{\tau}_1(x, y) = \rho g H \Pi, \quad \bar{\tau}_2(x, y) = 0, \quad (15)$$

$$\bar{q}_1(x, y) = F \left(\frac{|\bar{\tau}|}{(\rho_s - \rho) g D} \right) D \sqrt{\frac{\rho_s - \rho}{\rho} g D}, \quad \bar{q}_2(x, y) = 0. \quad (16)$$

3 Non-dimensionalization and Simplification

We list the main variables and define their scales (denoted by square brackets) in Table 1.

The scale for the bed-load flux $[\mathbf{q}]$ in our study differs from the classical scales, e.g., [77, 70] which use grain settling velocities. Since our model resolves vertical velocities, our proposed scaling is based on vertical gradients of the velocity.

Denoting the non-dimensionalized variables with stars, the non-dimensional forms of equations (1-9) are given by,

$$\nabla \cdot \mathbf{u}^* = 0, \quad \text{on} \quad r^* < z^* < 2, \quad (17)$$

$$\gamma \frac{\partial \mathbf{u}^*}{\partial t^*} = -\mathbf{u}^* \cdot \nabla \mathbf{u}^* + \frac{1}{\text{Re}} \left[\nabla^2 \mathbf{u}^* - \frac{2}{\Pi} \nabla p^* + \frac{2}{\Pi} \mathbf{g}^* \right], \quad \text{on} \quad r^* < z^* < 2, \quad (18)$$

$$\frac{\partial r^*}{\partial t^*} = -\nabla \cdot \mathbf{q}^*, \quad \mathbf{q}^* = \kappa F(S|\boldsymbol{\tau}^*|) \hat{\boldsymbol{\tau}}, \quad F(S|\boldsymbol{\tau}^*|) = 8(S|\boldsymbol{\tau}^*| - \tau_c^*)^{1.5}, \quad (19)$$

$$\mathbf{u}^* = \mathbf{0}, \quad p^* = \frac{p_a}{\rho g H} + \sigma_i \frac{Z_0}{H} \cos \beta - \sigma_i x^* \cos \beta \tan \alpha, \quad \text{at} \quad z^* = 2, \quad (20)$$

$$u^* = 0, \quad v^* = 0, \quad w^* = L\gamma \frac{\partial r^*}{\partial t^*}, \quad \text{at} \quad z^* = Lr^*, \quad (21)$$

where $\mathbf{g}^* = (\sin \beta, 0, -\cos \beta)$, Re is the Reynolds number, L is the grain-to-film size ratio, σ is the grain-to-fluid density ratio, γ is the hydrology-to-sediment transport time scale ratio, S is the steady state non-dimensional bed stress, also known as Shields number, and κ is a non-dimensional constant for the bed-load

Table 1: Characteristic scales of system variables.

| Variable | Scale | Description |
|-----------------------|--|---|
| $[x], [y], [z]$ | H | The coordinate system scales with the film thickness. |
| $[h]$ | H | The ice-water interface, which is considered a fixed boundary, is at distance $2H$ from the till-water boundary. |
| $[r]$ | D | The evolution of the till-water interface is governed by an active bed-load transport layer that is a few grain diameters in thickness [28, 36]. |
| $[\mathbf{u}]$ | $\frac{H^2 g \Pi}{2\nu}$ | The steady state solution (13) determines this velocity scale as a balance between shear stress and hydraulic gradient. |
| $[\boldsymbol{\tau}]$ | $\rho g H \Pi$ | The bed stress scale is derived from (8). |
| $[p]$ | $\rho g H$ | This scaling is consistent with the hydrostatic and cryostatic pressures within the fluid. |
| $[\mathbf{q}]$ | $\frac{\rho_s}{\rho} D \frac{D}{H} [\mathbf{u}]$ | The bed-load flux is defined to scale with sediment density ($\sim \sigma$), bed-load layer thickness ($\sim D$) and near-bed fluid velocity ($\sim \frac{D}{H} [\mathbf{u}]$). |
| $[t]$ | $(1 - \phi_m) \frac{DH}{[\mathbf{q}]}$ | This characteristic time scale is defined according to the Exner equation (6) and describes the rate of sediment transport. |

functional,

$$\mathbf{L} = \frac{D}{H}, \quad \text{Re} = \frac{[\mathbf{u}] H}{\nu}, \quad \sigma = \frac{\rho_s}{\rho}, \quad \gamma = \frac{H}{[\mathbf{u}] [t]}, \quad \mathbf{S} = \frac{[\boldsymbol{\tau}]}{(\rho_s - \rho)gD}, \quad \kappa = \frac{D\sqrt{(\sigma - 1)gD}}{[\mathbf{q}]}.$$

(22)

The main dimensional parameters of the system, $H, D, \beta, \alpha, \Pi, \rho, \rho_s, \rho_i, \phi_m, g, \nu, \tau_c^*$, reduce to the following independent dimensionless quantities, $\text{Re}, \mathbf{L}, \beta, \alpha, \sigma, \sigma_i, \phi_m, \tau_c^*$. We do not include the terms p_α and Z_0 as parameters since they only contribute to the ambient pressure in (20) and do not affect the dynamics of the system. The dependent dimensionless quantities are given by,

$$\gamma = \frac{\mathbf{L}\sigma}{1 - \phi_m}, \quad \mathbf{S} = \frac{\Pi}{(\sigma - 1)\mathbf{L}}, \quad \kappa = \frac{\sqrt{2(\sigma - 1)}}{\sigma\sqrt{\text{Re}\mathbf{L}\Pi}}, \quad \Pi = \sigma_i \tan \alpha \cos \beta + \sin \beta.$$

(23)

Among the eight independent non-dimensional quantities, the latter four, $\sigma, \sigma_i, \phi_m, \tau_c^*$ tend to vary by less than an order of magnitude over the range of subglacial settings. We represent them with constant values as given in Table 2. We also assume that the bed slope and surface slope are roughly comparable, i.e., $\beta \sim \alpha$, which is justified by observational records, e.g., [21, 15]. This allows us to simplify the driving force parameter Π in (11),

$$\Pi \approx 2 \sin \alpha.$$

(24)

Summarizing, the system is determined by three non-dimensional parameters Re, L and α where Re represents the fluid flux, L governs the hydrology-to-sediment transport time scale ratio, and α characterizes the fluid driving force.

Table 2: Fundamental parameters of the model, along with their estimates and ranges.

| Parameter | Estimate/Range | Description |
|------------|---|--|
| H | $10^{-4} \text{ m} \leq H \leq 10^{-2} \text{ m}$ | Film thickness (divided by 2). Values based on observations [32] and drainage theory [14]. |
| D | $10^{-6} \text{ m} \leq D \leq 10^{-4} \text{ m}$ | Grain diameter. Core measurements [67] reveal a bi-modal clay ($D \sim 1\mu\text{m}$) and sand distribution ($D \sim 100\mu\text{m}$). |
| β | $10^{-4} \leq \beta \leq 0.1$. | Bed slope angle. Values from [21]. The large range allows our model to consider both the polar and alpine settings. |
| α | $10^{-4} \leq \alpha \leq 0.1$. | Ice surface slope angle. Values from [21]. |
| g | 9.8 ms^{-2} | Gravitational acceleration near the Earth's surface. |
| ν | $1.787 \times 10^{-6} \text{ m}^2\text{s}$ | Kinematic viscosity of water at 0° C . |
| ρ | 1000 kgm^{-3} | Density of water at 0° C . |
| ρ_s | 2600 kgm^{-3} | Density of sediment grains, assuming clay-like material. |
| ρ_i | 917 kgm^{-3} | Density of ice. |
| ϕ_m | 0.4 | Mean porosity of subglacial sediment [68]. |
| τ_c^* | 0.12 | Threshold Shields stress. Empirical value [10, 55, 36]. |
| Z_0 | $0.1 \text{ km} \leq Z_0 \leq 4 \text{ km}$ | Characteristic glacier thickness [15]. For alpine glaciers $Z_0 \sim 100 \text{ m}$. For Antarctic ice sheets $Z_0 \sim 1 \text{ km}$. |
| L | $10^{-4} \leq L \leq 10^{-2}$ | Grain-to-film size ratio. Our model assumes $L \ll 1$. |
| σ | 2.6 | Grain-to-fluid density ratio. |
| Re | $Re < 10^4$ | Reynolds number. We assume a non-turbulent regime. |

We assume that sediment grains are very small compared to the film size, i.e., $L \ll 1$. In that case, (23) implies that $\gamma \ll 1$ and makes the till-water boundary conditions (21) homogeneous,

$$w^* = L\gamma \frac{\partial r^*}{\partial t^*} = O(L^2) \sim 0. \quad (25)$$

4 Applicability of the Model

Since glacial settings are diverse it is valuable to clarify where the assumptions and scaling choices within our model are applicable. In this section we present

plots of parameter spaces and identify regions of the parameter space that lie within the scope of our model.

One of the key requirements of our model is maintaining a low-to-intermediate Reynolds number for the film flow ($Re < 10^4$). Since the Reynolds number, defined in (22), is governed by the film thickness scale H and the surface slope α , due to (24), we plot contours of Re against these parameters in Figure 2(a). The range of surface slopes aims to capture both the polar setting, especially the Siple Coast, West Antarctica (e.g., $\alpha \sim 0.001$ [21]) as well as the alpine setting which is characterized by steeper slopes. The red shaded region highlights $Re > 10^4$ which we consider as the turbulent regime. Our model is only applicable to non-turbulent films, which are on the order of centimeters in thickness or less, as per Figure 2(a). Observational evidence records films with thicknesses of $1\mu\text{m}$ to 0.1mm [33, 71], which is on the lower end of our parameter space. Theoretical studies generally assume films that are millimeters thick [72, 14].

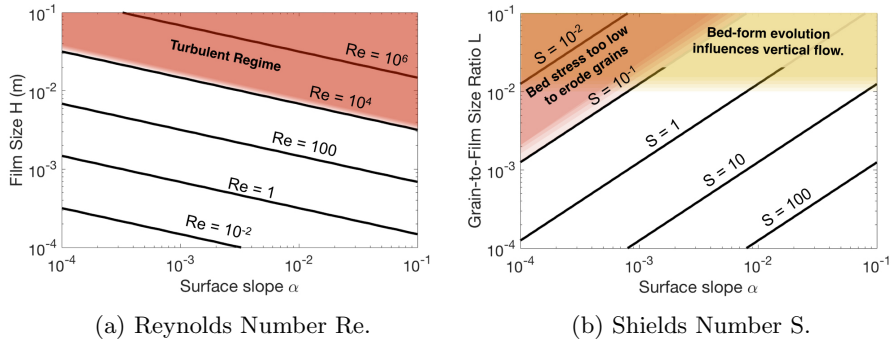


Figure 2: (a) Contour plot of Re for a given film size H and surface slope α . (b) Contour plot of the non-dimensional bed stress S for a given grain-to-film size L and surface slope α . The model is inapplicable within the shaded regions.

Active sediment transport at the bed of the film is a key prerequisite for potential channelization. This requirement can be described by the non-dimensional bed stress exceeding the critical Shields stress needed to erode sediment grains. Within our model, the non-dimensional bed stress S is a function of surface slope α and grain-to-film size ratio L , described in (22). Figure 2(b) shows the contour plots of S over the ranges of α and L . The region where the bed stress does not exceed the critical Shields threshold is represented by the red shaded triangle.

The parameter L also governs feedbacks between the bed and the vertical flow velocity as represented in the kinematic boundary condition (5). The assumption $L \ll 1$ enables us to ignore kinematic boundary effects in (25). The yellow shaded rectangle in Figure 2(b) highlights the region of $L > 10^{-2}$, which is beyond the scope of our model.

4.1 Competition between Ice Melt and Sediment Transport

The existing literature focuses primarily on the role of thermal processes in driving channelization of subglacial drainage [72, 75]. Comparatively less effort has been devoted to understanding the role of sediment transport processes in shaping subglacial hydrological systems over soft beds. Our study attempts to address this gap with the mechanical model outlined in Section 2 that couples hydrology and sediment transport. Since our model does not include thermal processes, its applicability is restricted to a regime where sediment transport is significantly faster than film-induced melting of the ice. We conduct a rudimentary comparison of time scales to identify the parameter space that characterizes this regime. To that aim, we introduce a simple thermal model for melting of the ice. Note that the presence of a subglacial meltwater film indicates a temperate basal setting, i.e., the base of the ice is at melting point. The energy balance at the ice-water interface is described by the Stefan equation,

$$L_H \rho_i \frac{\partial h}{\partial t} = Q^+ - Q^-, \quad (26)$$

where $L_H = 3.36 \cdot 10^5 \text{ J kg}^{-1}$ is the latent heat of fusion of water, Q^+ is the heat flux into the ice from the water along the direction normal to the interface, and Q^- is the analogous heat outflux.

The potential sources of heat influx Q^+ for subglacial settings are frictional heating of ice sliding over the bed, film thermal dissipation and geothermal heat flux [15]. Frictional heating is suppressed in the presence of a meltwater film which lubricates the ice-bed contact. Thermal dissipation within the film is negligible in non-turbulent settings. The main source of heat flux in our setting is geothermal, which is transported through the film to the ice-water interface. We assume that heat influx Q^+ scales with the geothermal heat flux G , i.e., $Q^+ \sim G$.

The heat outflux at the ice-water interface is a result of conduction through the ice. With the goal of deriving a conservative upper bound on the ice melt, we assume that the outflux is negligible compared to the influx, i.e., $Q^- = 0$. We derive the ice melt time scale $[t_i]$ using (26),

$$L_H \rho_i \frac{D}{[t_i]} = G, \quad (27)$$

where geothermal heat flux is assumed to be the dominant source of heat. We scale the evolution of the ice-water interface h by the sediment grain size D to make an appropriate comparison with the erosion-based evolution of the till-water interface.

The Exner equation (6) and the Stefan equation (26) highlight two processes for the evolution of a meltwater film. We compare the time scales of these two processes, namely ice melt and sediment transport, to identify which process is faster at carving out a channel. We represent the ratio of the time scales of

these two processes, $R = \frac{[t]}{[t_i]}$ defined in (27) and Table 1,

$$R = \frac{\nu(1 - \phi_m)G}{\sigma D^2 L_H \rho_i g \sin \alpha}. \quad (28)$$

We calculate R over our parameter space. Observational estimates for geothermal heat flux in the Siple coast region show a range of $0.04 \text{ Wm}^{-2} \leq G \leq 0.13 \text{ Wm}^{-2}$ [49]. Since the variation in G is less than an order of magnitude, we choose a representative value, $G = 0.13 \text{ Wm}^{-2}$. This higher end value provides a conservative upper bound for the rate of ice melt. We plot R as a function of surface slope α and grain diameter D in Figure 3, along with a constant geothermal heat flux value $G = 0.13 \text{ Wm}^{-2}$. The figure indicates sediment transport is several orders of magnitude faster than ice melt for most of the parameter space. The red shaded triangle denotes the region where R is close to 1, indicating that the model is inapplicable within the region. Overall, Figure 3 suggests that decoupling the dynamics of the ice-water interface from the meltwater film for the purposes of stability analysis is a suitable assumption for a large variety of glaciological settings.

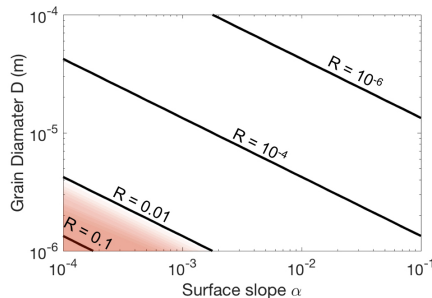


Figure 3: Contour plots of the time scales ratio, R , defined in (28). Geothermal heat flux $G = 0.13 \text{ Wm}^{-2}$. The red shaded region indicates $R > 0.01$ where the two time scales are comparable.

5 Linear Stability Analysis

To better understand the stability of a subglacial meltwater film flowing over a sediment bed, we perform a linearized stability analysis on the model presented in Section 3.

We consider small amplitude perturbations about the steady state (13) and expand dependent non-dimensional variables as,

$$f(x, y, z, t) = \bar{f}(z) + \varepsilon \tilde{f}(x, y, z, t), \quad \varepsilon \ll 1, \quad (29)$$

where barred quantities represent steady state variables, and for simplicity we have omitted stars denoting non-dimensional variables. In light of the domain

being infinitely extended in the x and y directions, we represent the perturbation as elements of the Fourier basis,

$$\tilde{f}(x, y, z, t) = \hat{f}(z, t) \exp(ik_1x + ik_2y), \quad (30)$$

where k_1, k_2 are the wavenumbers of the perturbations in the x - and y - directions respectively. Given the linearity of the system, we also assume separation of variables in z and t , so that,

$$\hat{f}(z, t) = f'(z) \exp(\omega t), \quad \omega = \omega_r + i\omega_i. \quad (31)$$

where w_r and w_i are the real and imaginary parts of ω respectively. Note that the sediment flux \mathbf{q} and bed-form r do not vary along the depth, hence the variables r' and \mathbf{q}' are independent of z .

The sign of the real part of ω is the key indicator of stability within the meltwater film. If $\omega_r > 0$, then the perturbation in the system described by wavenumbers (k_1, k_2) undergoes exponential amplification with time. As long as the bed is perturbed as well, i.e., $r' \neq 0$, it would experience similar amplification for $\omega_r > 0$. We interpret such unstable bed-form growth as subglacial channel initiation. The goal of the linear stability analysis is to compute ω_r given model parameters and perturbation wavenumbers k_1, k_2 . If there exists a perturbation (k_1, k_2) for which $\omega_r > 0$, then the system is deemed unstable.

We introduce small amplitude perturbations described in (31) and linearize the equations (17- 21) around the steady state. Denoting the derivative $\frac{d}{dz}$ by D , we obtain the equations,

$$0 = ik_1u' + ik_2v' + Dw', \quad \text{on } 0 < z < 2, \quad (32)$$

$$\gamma\omega u' = -ik_1\bar{u}u' - wD\bar{u} - \frac{2ik_1}{\Pi\text{Re}}p' + \frac{1}{\text{Re}}[-k_1^2 - k_2^2 + D^2]u', \quad \text{on } 0 < z < 2, \quad (33)$$

$$\gamma\omega v' = -ik_1\bar{u}v' - \frac{2ik_1}{\Pi\text{Re}}p' + \frac{1}{\text{Re}}[-k_1^2 - k_2^2 + D^2]v', \quad \text{on } 0 < z < 2, \quad (34)$$

$$\gamma\omega w' = -ik_1\bar{u}w' - \frac{2}{\Pi\text{Re}}Dp' + \frac{1}{\text{Re}}[-k_1^2 - k_2^2 + D^2]w', \quad \text{on } 0 < z < 2, \quad (35)$$

$$0 = u', \quad 0 = v', \quad 0 = w', \quad 0 = p', \quad \text{at } z = 2, \quad (36)$$

$$0 = u' + Lr'D\bar{u}, \quad 0 = v', \quad 0 = w', \quad \text{at } z = 0, \quad (37)$$

$$\omega r' = -ik_1\text{Skd}F [Du' + ik_1w'] - ik_2\kappa F [Dv' + ik_2w'], \quad \text{at } z = 0, \quad (38)$$

where, F and $\frac{dF}{d|\bar{\tau}|}$ are steady state sediment transport values derived via (19) for $\bar{\tau} = (1, 0)$,

$$F = F(S|\bar{\tau}|) = A(S-0.12)^m, \quad dF = dF(S|\bar{\tau}|) = Am(S-0.12)^{m-1}, \quad A = 8, \quad m = 1.5. \quad (39)$$

Since the bed-load transport functional (9) is non-differentiable at the threshold for initiating grain erosion, it is mathematically necessary that the system always exceed the threshold so that we can linearize the sediment transport equations for the perturbations around the steady state.

In (37), the no-slip boundary conditions (21) at the moving boundary $z = r$ have been transformed by a Taylor expansion in ε into equivalent boundary conditions imposed at the domain boundary $z = 0$. The equivalence allows us to solve the system of equations on a fixed domain while obtaining the solution to the original problem with an evolving till-water interface.

5.1 Reformulation in Terms of Streamfunction

The perturbation introduced into the steady state is two-dimensional in nature, described by the wavenumbers k_1 and k_2 . To simplify our analysis, we reduce the perturbation to a single dimension. The Squire transformation [20, 5, 30] is a classical method that projects three-dimensional fluid flow onto a plane while preserving its perturbation characteristics. This plane, known as the Squire plane, is defined by the z -axis, and the vector (k_1, k_2) in the horizontal plane. We define k as the Squire perturbation wavenumber, θ as the Squire angle, and \mathcal{U} as the horizontal velocity in the (k_1, k_2) direction, such that,

$$k_1 = k \sin \theta, \quad k_2 = k \cos \theta, \quad k\mathcal{U}' = k_1 u' + k_2 v'. \quad (40)$$

We take appropriate linear combinations of equations (32-37) to replace u' and v' with \mathcal{U}' ,

$$0 = ik\mathcal{U}' + Dw', \quad \text{on } 0 < z < 2, \quad (41)$$

$$\gamma\omega\mathcal{U}' = -ik_1\bar{u}\mathcal{U}' - ik_1D\bar{u}w' - \frac{2ik}{\Pi\text{Re}}p' + \frac{1}{\text{Re}}[-k^2 + D^2]\mathcal{U}', \quad \text{on } 0 < z < 2, \quad (42)$$

$$\gamma\omega w' = -ik_1\bar{u}w' - \frac{2}{\Pi\text{Re}}Dp' + \frac{1}{\text{Re}}[-k^2 + D^2]w', \quad \text{on } 0 < z < 2, \quad (43)$$

$$\mathcal{U}' = 0, \quad w' = 0, \quad p' = 0, \quad \text{at } z = 2, \quad (44)$$

$$k\mathcal{U}' = -k_1LD\bar{u}r', \quad w' = 0, \quad \text{at } z = 0. \quad (45)$$

The Exner equation (38) does not map perfectly onto the \mathcal{U}' and w' notation since the coefficients of $k_1 u'$ and $k_2 v'$ are not equal. We remedy this anomaly by assuming that $\theta \ll 1$, i.e., $k_1 \ll k_2$. This allows us to add and subtract terms of the type $O(k_1)$ so that we can replace the term $ik_1\text{Skd}F[Du' + ik_1w']$ with $ik_1\kappa F[Du' + ik_1w']$ to yield,

$$\omega r' = -ik\kappa F[D\mathcal{U}' + ikw'], \quad \text{at } z = 0. \quad (46)$$

The assumption $k_1 \ll k_2$ means that the along-flow perturbations have very long wavelengths compared to the across-flow perturbations. These are precisely the type of perturbations we are interested in, since the formation of channels that run along x -direction requires bed-form structure in the y -direction. Note that setting $k_1 = 0$, i.e., $\theta = 0$, completely removes the influence of the steady state from the above equations, effectively rendering the linear stability analysis inconclusive. We generally choose $\theta = 0.01$.

We introduce a streamfunction ψ so that mass balance (41) holds implicitly,

$$\mathcal{U}' = D\psi, \quad w' = -ik\psi. \quad (47)$$

Streamfunction notation allows us to eliminate the pressure term and reformulate our equations into the Orr-Sommerfeld (OS) equation [5, 20, 54],

$$\gamma\omega [D^2 - k^2] \psi = -ik_1 [\bar{u}D^2\psi - \psi D^2\bar{u} - k^2\bar{u}\psi] + \frac{1}{\text{Re}} [D^2 - k^2]^2 \psi, \quad \text{on } 0 < z < 2. \quad (48)$$

The boundary equations arise from (44), (45) and (46),

$$D\psi = 0, \quad \psi = 0, \quad \text{at } z = 2, \quad (49)$$

$$D\psi = -\sin(\theta)LD\bar{u}r', \quad \psi = 0, \quad \text{at } z = 0, \quad (50)$$

$$\omega r' = -ik\kappa FD^2\psi \quad \text{at } z = 0. \quad (51)$$

In deriving (51) we have used the boundary condition $\psi(0) = 0$.

Given k_1 and k_2 , we compute ω_r by solving (48) with boundary conditions (49), (50), and boundary evolution (51) for the unknowns ψ, r' and ω . Note that we can normalize r' as $r' = 1$.

5.2 Numerics

We reformulate the system of equations (48), (49), (50) and (51) as an eigenvalue problem and solve numerically to obtain the eigenvalue-eigenvector pairs ω and (ψ, r') . To discretize the system of equations, we use a spectral Galerkin method originally proposed by Shen et al. [63] and adapted for the current problem from [8, 9]. We express the stream-function as a linear combination of doubly integrated Legendre polynomials that vanish at the boundaries, plus two low order polynomials that incorporate the till-water boundary conditions. We present the details of the discretization in the Supplementary Material.

The key benefit of Spectral Galerkin methods is that numerical accuracy does not depend on spatial discretization, but on the number of spectral elements. This method is particularly well-suited to our physical system where spatial resolution of the near-bed dynamics, especially the computation of the derivatives $D^2\psi$ in (51), is crucial for determining bed stability. Spectral Galerkin methods are known to be highly accurate for solving the OS equation with homogenous boundary conditions [42], with the key advantage of not producing spurious eigenvalues.

6 Results

We study the stability characteristics of the meltwater film for given parameters and perturbation wavenumber k . We solve the system of equations (48-51) to obtain the eigenvalue-eigenvector solutions ω and (ψ, r') respectively. Recall that the variable $\omega = \omega_r + i\omega_i$ represents the growth rate of the perturbation,

and $\omega_r > 0$ implies that the system is unstable. The function $\psi(z)$ is the perturbed streamfunction, and r' characterizes the amplitude of the bed-form perturbation.

The system of equations (48-51) exhibits an infinite number of eigenvalue-eigenvector solutions ω and (ψ, r') for any given wavenumber k . These eigenpairs represent a variety of states that the system can exist in for a given perturbation. These states and their superimpositions characterize the various responses, to linear order, of the coupled hydrodynamics and sediment transport of the system to the imposed perturbation. By solving the discretized system, we numerically compute a finite number of these solutions, equal to the number of equations in the discretized system. From now on, ω, ψ, r' refer to the solutions of the discretized equations.

6.1 System Instability

We consider a meltwater film with the following parameter values: Reynolds number $Re = 20$, grain-to-film size ratio $L = 10^{-3}$ and surface slope $\alpha = 0.001$. This system corresponds to film thickness $2H \approx 4\text{mm}$ and grain diameter $D \approx 2\mu\text{m}$. We discretize the system with number of spectral elements $N = 300$ and plot the spectra of eigenvalues in Figure 4(a) for wavenumbers $10^{-3} \leq k \leq 10^3$. For each wavenumber k on the x-axis, we plot on the y-axis the top fifty eigenvalues with the largest real parts. We indicate the sign of ω_r by open circles (positive) and dots (negative). Figure 4 remains qualitatively similar over the ranges of parameters Re, L and α .

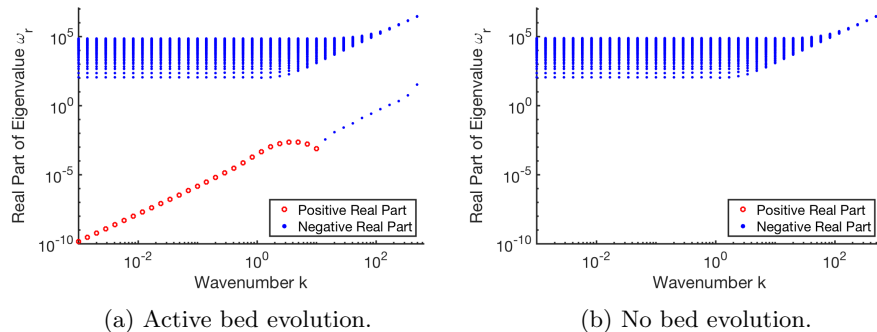


Figure 4: Plot of real parts of the eigenspectra for $Re = 20, L = 10^{-3}, \alpha = 10^{-3}$. (a) Spectra for the standard system of equations. The eigenvalue isolated at the bottom corresponds to the sediment transport eigenvalue. (b) The Exner equation (51) is replaced by $\omega = 0$.

Most of the spectra lie in the upper half of Figure 4(a) and has negative real part. One eigenvalue stands out in magnitude. This distinctive eigenvalue arises because of the significant difference between the times scales of hydrology and sediment transport ($\gamma \ll 1$). In the system of equations, since the sedi-

ment transport equation (51) is the only equation where γ does not multiply ω , that equation yields an eigenvalue of relatively smaller magnitude. We refer to this particular eigenvalue as the sediment transport eigenvalue, since it corresponds to bed-form evolution. Its positive real part indicates a morphological instability.

We test the hypothesis that the distinctive eigenvalue represents the bed-form instability. We replace the Exner equation (51) with $\omega r' = 0$ which completely nullifies bed evolution. The corresponding spectra in Figure 4(b) show that the distinctive eigenvalue has disappeared from the plot while leaving the other eigenvalues unchanged, supporting our claim that the eigenvalue in Figure 4(a) with the smallest magnitude represents the bed-form instability.

The stability of the system is determined by the interplay of three physical processes within the OS equation (48), namely acceleration, advection, and diffusion,

$$\underbrace{\gamma \omega [D^2 - k^2]}_{\text{Acceleration}} \psi = \underbrace{-ik_1 [\bar{u}D^2 - D^2\bar{u} - k^2\bar{u}]}_{\text{Advection}} \psi + \frac{1}{\text{Re}} \underbrace{[D^2 - k^2]^2}_{\text{Diffusion}} \psi. \quad (52)$$

We investigate how these processes affect the stability of the system at different wavenumbers k .

6.2 Diffusion Causes Bed-form Migration

We first study a diffusion-only system where we suppress the advection ($\text{Re} \ll 1$) and acceleration ($\gamma \ll 1$). We numerically solve the system of equations (48-51) and we isolate the sediment transport eigenvalue ω , and the corresponding streamfunction ψ , as the eigenvalue with the smallest magnitude. Figure 5 highlights the velocity and shear stress perturbations which are solutions to the system of equations. Panels (a) and (c) consider the case $k = 1$ and show the Squire velocity vector field (\mathcal{U}, w) , as well as the color plots of \mathcal{U} and the perturbation of the shear stress,

$$\tau = D^2\psi. \quad (53)$$

The solid line represents the till-water interface perturbation, where its amplitude is not to scale since perturbations within our study are infinitesimal. Panels (b) and (d) represent short wavelength perturbation regime ($k = 10$).

The horizontal velocities at the till-water interface are generated by the bed perturbation as described by (50). The velocities then diffuse toward the ice, and their corresponding derivatives create the stress field. The near-bed vertical velocities and associated circulation cells are generated by mass conservation over the horizontal velocity gradients at the boundary.

Figure 5 shows that bed-stress and bed-form are in phase, in which case (51) indicates that the real part of the sediment transport eigenvalue is zero. Since the system perturbations have the form $\exp(k_1x + k_2y + \omega t)$, the fact that $\omega_r = 0$ implies that the bed-form neither amplifies nor decays, but simply

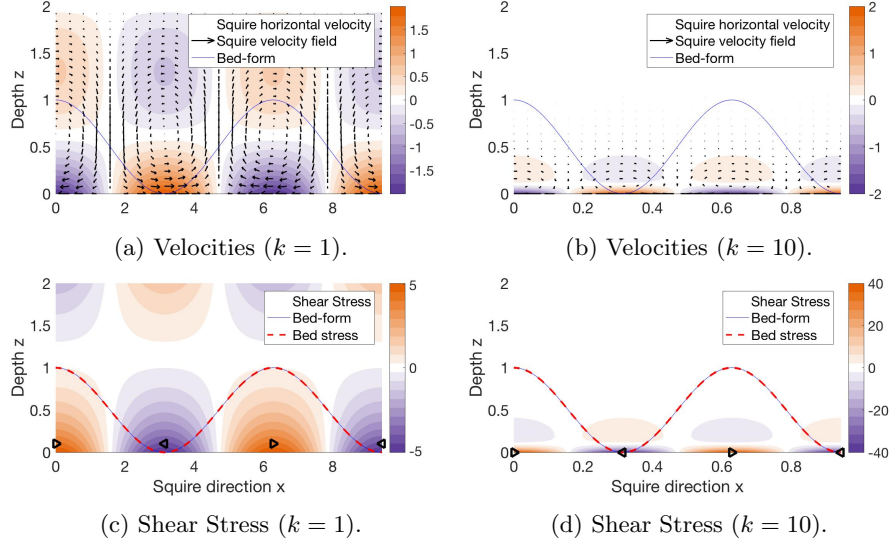


Figure 5: Solution for the diffusion-only case: no fluid advection or acceleration, $Re, \gamma = 10^{-6}$ and $F, L, \kappa, \theta = \frac{\pi}{2}$. (a) shows the velocity field and the color plot of Squire horizontal velocity \mathcal{U} for the long wavelength regime ($k = 1$). (c) shows the shear stress τ in the Squire direction for $k = 1$. The triangle markers indicate the sign of the stress (right-ward pointing stands for positive values). (b) and (d) represent the short wavelength regime ($k = 10$). The solid line represents the bed-form perturbation. Its amplitude is not to scale.

migrates along the bed. Thus suggests that diffusion by itself does not affect the stability of the system. In other words, a diffusion-only system is neutrally stable.

We develop a reduced model to better understand the physics in the diffusion-only case that leads to $\omega_r = 0$. Figure 5(b) suggests the formation of a boundary layer for the short wavelength regime ($k \gg 1$). We assume the following re-scaling of variables,

$$z^* = kz, \quad \psi^* = \frac{k\psi}{L \sin \theta}, \quad \omega^* = \frac{\omega}{k^2 F \kappa L \sin \theta}. \quad (54)$$

The re-scaled OS equation (48) takes the form,

$$a_1 \omega (D^2 - 1) \psi^* = -i a_2 \left[(2z^* - k^{-1} z^{*2}) (D^2 - 1) + 2k^{-1} \right] \psi^* + (D^2 - 1)^2 \psi^*, \quad (55)$$

$$\text{where, } a_1 = FL\gamma Re \kappa \sin \theta, \quad a_2 = Re k^{-2} \sin \theta. \quad (56)$$

The limits $a_1 \rightarrow 0$ and $a_2 \rightarrow 0$ to suppress acceleration and advection. We perform an asymptotic expansion of the variables to study the short wavelength regime,

$$z^* = z^{(0)} + O(k^{-1}), \quad \psi^* = \psi^{(0)} + O(k^{-1}), \quad \omega^* = \omega^{(0)} + O(k^{-1}), \quad k \gg 1. \quad (57)$$

We reduce the equations (55), (50), (49) and (51) to leading order as $k \rightarrow \infty$,

$$0 = (D^2 - 1)^2 \psi^{(0)}, \quad \text{on } 0 < z^{(0)} < \infty, \quad (58)$$

$$D\psi^{(0)} = -2, \quad \psi^{(0)} = 0, \quad \text{at } z^{(0)} = 0, \quad (59)$$

$$D\psi^{(0)} \rightarrow 0, \quad \psi^{(0)} \rightarrow 0, \quad \text{as } z^{(0)} \rightarrow \infty, \quad (60)$$

$$\omega^{(0)} = -iD^2\psi^{(0)} \quad \text{at } z^{(0)} = 0. \quad (61)$$

The leading order solution of the reduced boundary layer model is given by,

$$\psi^{(0)} = -2z^{(0)} \exp(-z^{(0)}), \quad \omega^{(0)} = -4i, \quad (62)$$

Comparison between the analytical and the re-scaled numerical solutions show good agreement (see Supplementary Material Figure S1). The above analysis supports the hypothesis that $\omega_r = 0$ to leading order in the short wavelength regime, which implies that diffusion by itself is neutrally stable, i.e., it does not affect the stability of the system.

In the long wavelength regime ($k \ll 1$), we consider the following re-scaled variables,

$$\psi^* = \frac{\psi}{L \sin \theta}, \quad \omega^* = \frac{\omega}{FLk\kappa \sin \theta}, \quad (63)$$

to obtain the re-scaled OS equation,

$$b_1 k \omega^* (D^2 - k^2) \psi^* = -ib_2 k [(2z - z^2) (D^2 - k^2) + 2] \psi^* + (D^2 - 1)^2 \psi, \quad (64)$$

$$\text{where, } b_1 = FL\gamma \text{Re} k \sin \theta, \quad b_2 = \text{Re} \sin \theta. \quad (65)$$

The advection and acceleration terms automatically vanish as $k \rightarrow 0$. We consider the asymptotic expansion of the system at $k = 0$,

$$z = z^{(0)} + O(k), \quad \psi^* = \psi^{(0)} + O(k), \quad \omega^* = \omega^{(0)} + O(k), \quad k \ll 1. \quad (66)$$

The equations (48-51) as $k \rightarrow 0$, to leading order, read as,

$$0 = D^4 \psi^{(0)}, \quad \text{on } 0 < z < 2, \quad (67)$$

$$D\psi^{(0)} = -2, \quad \psi^{(0)} = 0, \quad \text{at } z^{(0)} = 0, \quad (68)$$

$$D\psi^{(0)} = 0, \quad \psi^{(0)} = 0, \quad \text{as } z^{(0)} = 2, \quad (69)$$

$$\omega^{(0)} = -iD^2\psi^{(0)} \quad \text{at } z^{(0)} = 0. \quad (70)$$

Omitting the asymptotic notation, the leading order solution is given by,

$$\psi = -2z + 2z^2 - \frac{1}{2}z^3, \quad \omega = -4i, \quad (71)$$

and shows that $\omega_r = 0$ as $k \rightarrow 0$, which implies that the diffusion-only system is neutrally stable.

6.3 Advection Destabilizes the System

We study the role of advection-diffusion interaction in the instability by considering a set of parameters that suppress acceleration ($\gamma \ll 1$). Figure 6 shows plots velocity and shear stress for the advection-diffusion regime. The computed velocity field exhibits a right-ward skew. This skew causes leads a left-ward phase shift of the shear stress, especially the bed stress, providing a phase advance over the bed-form. The bed stress advancing ahead of the bed-form implies that $\text{Im}(\tau) > 0$ which yields $\omega_r > 0$ from (51) and (53), suggesting that advection contributes to the instability of the system.

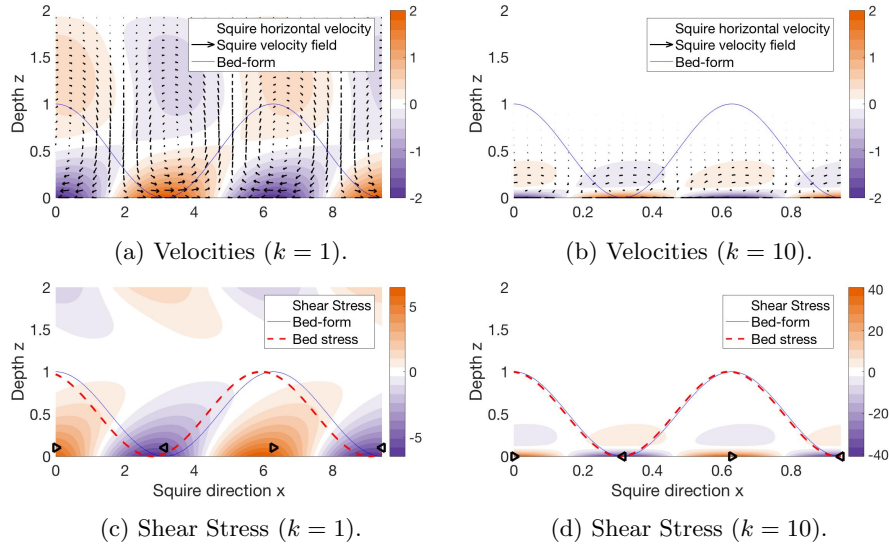


Figure 6: Advection creates a right-ward skew of velocity and phase advance of the shear stress. Solution of the system for the advection-diffusion case, $Re = 20$, $\gamma = 10^{-6}$ and $F, L, \kappa = 1$. $\theta = \frac{\pi}{2}$. (a) and (b) represent the long wavelength regime with $k = 1$. (c) and (d) represent the short wavelength regime with $k = 10$. The solid line represents the bed-form perturbation. Its amplitude is not to scale.

We use a reduced model to test our hypothesis that the advection-diffusion force balance leads to $\omega_r > 0$ in the short wavelength regime. We take the limit $a_1 \rightarrow 0$ of the re-scaled OS equation (55) to suppress the acceleration term. The short wavelength asymptotic expansion (57) yields,

$$2ia_2 z^{(0)}(D^2 - 1)\psi^{(0)} = (D^2 - 1)^2\psi^{(0)}, \quad \text{on } 0 < z^{(0)} < \infty, \quad (72)$$

while the boundary equations are identical to the short wavelength diffusion

case, (59-61). The leading order solution is given by,

$$\psi^{(0)} = \frac{2 \int_0^z \int_v^\infty e^{2v-s-z} \text{Ai}(c^{-1}s + c^2) ds dv}{\int_0^\infty e^{-s} \text{Ai}(c^{-1}s + c^2) ds}, \quad \omega^{(0)} = \frac{-2i \text{Ai}(c^2)}{\int_0^\infty e^{-s} \text{Ai}(c^{-1}s + c^2) ds}, \quad (73)$$

where $c = \frac{1}{\sqrt[3]{2ia_2}}$ with $\arg(c) = -\frac{\pi}{6}$, and $\text{Ai}(s)$ is one of the two standard linearly independent solutions of the system $D^2 f = sf$. The integrals in (73) converge as a consequence of the exponential decay rate of $\text{Ai}(s)$ for $-\frac{\pi}{3} < \arg(s) < \frac{\pi}{3}$.

The Supplementary Material Figure S3 shows good agreement between the re-scaled numerical solutions and the analytical solutions given by (73). Our finding that the real part of the analytical eigenvalue is positive supports our hypothesis that the interplay of advection and diffusion causes the instability.

In the long wavelength regime, the asymptotic analysis from the previous section suggests that diffusion dominates at long wavelengths, yielding a neutrally stable system, i.e., $\omega_r = 0$. Assuming that the sediment transport eigenvalue varies continuously with the wave number k , if $\omega_r > 0$ at some short wavelength, then it is likely that as $k \rightarrow 0$ the real part of the eigenvalue simply decays to 0 while maintaining its sign. This hypothesis indeed seems to hold in the Figure 4, where ω_r peaks at $k = 0.1$ and converges to 0 as k becomes small. The Supplementary Material provides more details.

We represent the physics of destabilization via advection in Figure 8(a). The steady state velocity \bar{u} advects momentum to the perturbed velocity field, causing the rightward skew that leads to a phase advance in the bed stress which amplifies the bed-form perturbations.

6.4 Fluid Acceleration Stabilizes the System for Short Wavelengths

The computed spectra in Figure 4(a) show that the real part of the sediment transport eigenvalue becomes negative as wavenumber becomes large, indicating that there is short-wavelength stabilization. Since our analysis suggest that advection is a destabilizer and diffusion by itself does not influence stability, we study the role of acceleration as a potential stabilizer.

We consider a regime of short wavelength ($k \gg 1$) and comparatively low Reynolds number ($\text{Re} = 1$) to partially suppress advection while maintaining the influence of acceleration ($\gamma = 0.5$). Figure 7 shows plots of computed velocity fields and shear stresses for this parameter regime. In contrast with the right-ward velocity skew in the advection-diffusion case, Figure 7(a) highlights a left-ward velocity skew, which creates a right-ward phase shift of the bed stress. The bed stress lagging behind the bed-form implies that $\text{Im}(\tau) < 0$, and hence yields $\omega_r < 0$. This suggests that acceleration contributes to the stability of the system.

We study the nature of the stabilization for the short wavelength regime with a reduced model. We follow the same recipe outlined in the previous subsections in (54) and (57). The limit $k \rightarrow \infty$ of the reduced OS equation (55) removes all

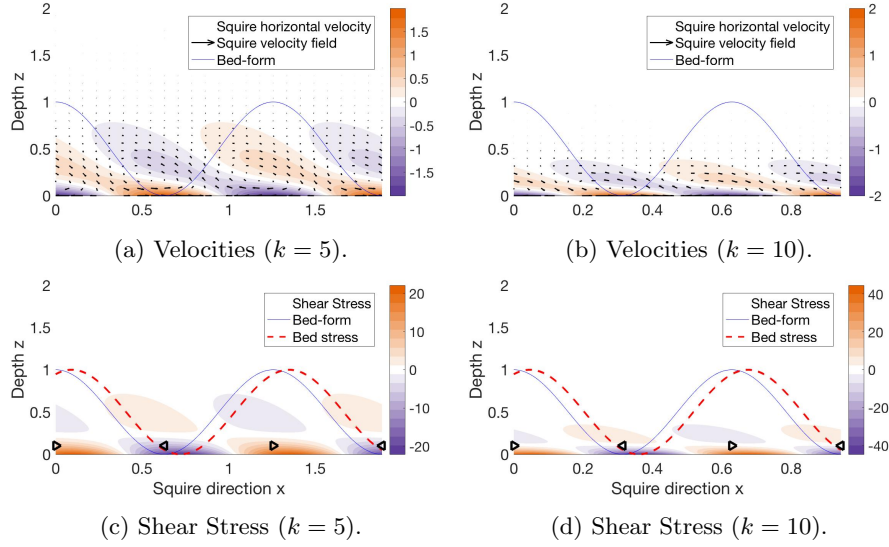


Figure 7: Acceleration creates a left-ward skew of velocity and phase lag of the bed stress. Solution of the system for low Reynolds number and short wavelength: $\text{Re}, F, L = 1$. $\theta = \frac{\pi}{2}$. $\gamma = 0.5$. (a) $k = 5$. (b) $k = 10$. Plot analogous to Figure 5.

the advection terms,

$$a_1 \omega (D^2 - 1)^2 \psi^{(0)} = (D^2 - 1)^2 \psi^{(0)}, \quad \text{on } 0 < z < \infty. \quad (74)$$

Omitting the asymptotic notation, the leading order solution of (74) and (59-61) is given by,

$$\psi = \frac{2i}{a_1} \left(e^{-z(1-ia_1)} - e^{-z} \right), \quad \omega = -2a_1 - 4i, \quad (75)$$

where we note that $\omega_r < 0$. This analysis suggests that the interaction between acceleration and diffusion stabilizes the system for short wavelengths.

We summarize the physical intuition for the stabilizing effect of acceleration in Figure 8(b). The key insight is that as the hydrology and sediment transport time-scales become comparable ($\gamma \sim 1$) the diffusion speed for fluid momentum becomes comparable to the speed of bed-form migration. The relative motion between the fluid velocities that diffuse toward the ice and the bed-form migration results in a left-skew of the velocity. This creates a corresponding phase lag in the bed stress that stabilizes the system. As the hydrology time scale becomes smaller ($\gamma \ll 1$), the velocity field adjusts itself more quickly to the moving bed-form, effectively reducing the skew. The limiting case of $\gamma \rightarrow 0$ completely removal of the skew and reduces the system to the diffusion-only case in Figure 5.

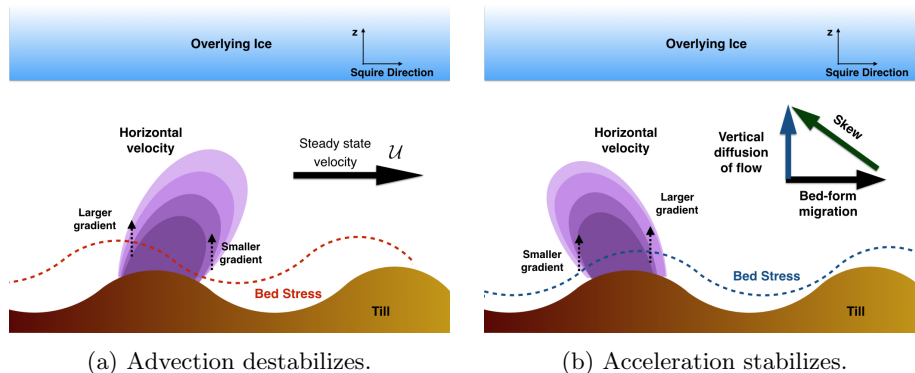


Figure 8: Representations of the physics for the stabilization and destabilization of the meltwater film caused by acceleration and advection respectively. Skews in the velocity field leads to phase shifts in the bed stress, which affect the stability of the system.

6.5 The Most Unstable Perturbation Wavelength

We define the wavenumber k_u as the one corresponding to the sediment transport eigenvalue with the largest positive real part. Since perturbations at this wavenumber grow at the fastest rate, the corresponding wavelength $\lambda_u = 2\pi k_u^{-1}$ is potentially indicative of the initial spacing between channels formed from the mechanisms of sediment transport described in this paper. To allow the comparison of this model against field observations, we perform a sensitivity study for λ_u over the three main parameters: Re, the Reynolds number; L, the grain-to-film size ratio, and α , the surface slope. We set $\theta = 0.01$ which implies that most of the perturbation is across-flow.

Figure 9 shows the results of the sensitivity analysis. The shaded red region on the left represents the regime where the bed stress is insufficient to erode the sediment since it is below the critical Shields threshold. The threshold increases with grain size as it becomes more and more difficult for the fluid to erode larger grains (see Figure 2(b)). This is reflected in Figure 9, where the region of no sediment transport is larger in panel (b) ($L = 10^{-2}$) than in (a) ($L = 10^{-3}$).

The four contour values of λ_u , 0.2, 0.5, 1, 3 are plotted as solid lines and span the range of the plot where the system is unstable. This suggests that the most unstable wavelength is either comparable or an order of magnitude smaller than the film thickness itself. The value of λ_u generally decreases with Re and increases with α . Comparing the two sub-figures suggests that λ_u is largely independent of L provided the non-dimensional bed stress S is large enough. The fastest growing wavelength stems from advection dominating acceleration. Based on the asymptotic analyses from the previous subsections, we measure the advection-acceleration competition through the ratio of coefficients $\frac{a_1}{a_2}$ and $\frac{b_1 k}{b_2 k}$ from the short (55) and long (64) wavelength regimes respectively. These

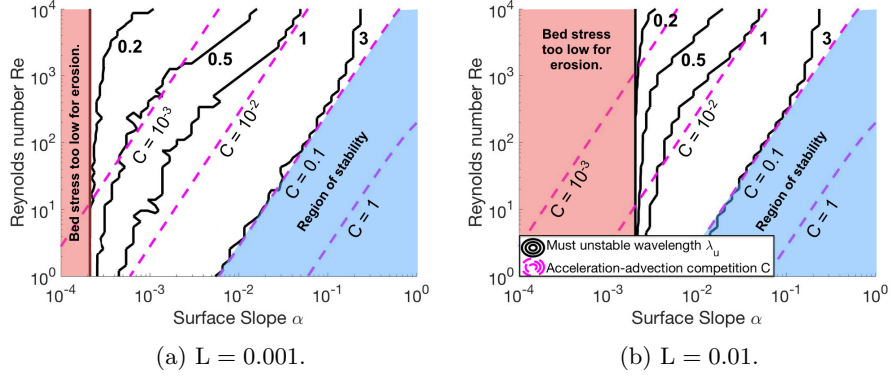


Figure 9: Contours of unstable wavelength λ_u over parameters Re and α . Solid line contours represent values of λ_u . The red shaded rectangular region indicates that the bed stress is insufficient to erode sediment. The shaded triangular blue region highlights a region of stability. (a) and (b) represent $L = 10^{-3}$ and $L = 10^{-2}$ respectively. The dashed magenta lines represent contours of C as per (76).

ratios simplify to the following condition for instability within the system, i.e., when advection dominates acceleration,

$$C \ll 1, \quad C = FL\kappa\gamma \approx \frac{2A\sqrt{2}\sin\alpha}{(\sigma-1)(1-\phi_m)\sqrt{Re}} \left(\frac{2\sin\alpha}{(\sigma-1)L} \right)^{m-1.5}. \quad (76)$$

In the above, we express γ, κ and $F \approx AS^m$ in terms of Re and α using (39) and (23).

We plot dashed line contours of C in Figure 9 with the classic Meyer-Peter-Müller values $A = 8$ and $m = 1.5$ [50]. The figure indicates that the region of stability roughly corresponds to $C \geq 0.1$, and that contours of the most unstable wavelength λ_u align with the contours of C provided that the system is well beyond the threshold Shields stress, i.e. away from the shaded red rectangular region. These findings support the idea that the advection-acceleration competition, as represented by C , is a measure of the system stability.

7 Discussion

We study subglacial channelization of meltwater films on soft beds using a mechanical model that couples hydrology and sediment transport. With a linearized stability analysis, we identify an instability where meltwater films grow by carving into the sediment layer beneath. This instability provides a potential mechanism to explain the formation of till-incised canals [73, 52]. We describe the physics of the channel initiation instability using the framework of flow over erodible beds [40, 11]. We show that the dynamics of the instability is similar to

that of ripple formation, where advective processes within the flow destabilize the system and cause bed-forms to grow. We also show that the hydrology of the system contains a stabilizing mechanism, namely flow acceleration, which dominates at short wavelengths. We discuss the implications of our work in the context of ripple instability dynamics and previous models of subglacial channel initiation.

7.1 Hydrodynamics Induces Short Wavelength Stabilization of Films

Instabilities of flow over erodible beds and the resulting evolution of bed morphology are classical topics in fluid dynamics and hydrology as reviewed, for example, by [40, 11]. Kennedy [39, 40] was among the first to explain the dynamics of the ripple formation instability. He identified that the instability arises from the phase advance of the bed shear stress over the bed-form, which is a result of near-bed flow advection being countered by the bed shear stress. However, the potential flow model used by Kennedy [39] aligned the bed-form and the bed stress exactly, thus requiring an externally imposed phase advance to activate the ripple instability. Shallow water models predicted stability of the bed at all wavelengths since they could not resolve the differences between mean flow and near-bed flow [47]. Rotational flow models which resolve the vertical flow velocities, e.g., [29, 59], addressed the phase advance problem successfully, and we follow this modeling approach to understand the evolution of meltwater films. Results from previous rotational flow models [29, 59, 13, 17] are consistent with the advection-induced instability mechanism discussed by Kennedy [39, 40] and presented in the current paper (see Figure 8(a)).

The theory of flow over erodible beds was originally intended for analyses of granular ripples on beaches and riverbeds [11]. Therefore, most film models assume a free surface boundary at the top [29, 59, 13]. Since our model represents meltwater films capped by ice, i.e., a fixed lid boundary condition, it does not exhibit the stabilizing effect of a free surface at subcritical flow [11], nor does it prompt the formation of antidunes at supercritical flow [13, 17]. The lack of stabilization from a free surface suggests that alternate mechanisms operate to stabilize films with fixed lids, a point that we will revisit shortly.

The direction of the bed-form presents another difference between our study and others. We focus on bed formations in the direction near-perpendicular to the flow because we are interested in the initiation of canals whose axes align with the film flow direction. Most previous studies [39, 29, 59], by contrast, analyze ripple formation along the film flow direction. Our results show that a change in the bed-form direction simply projects the dynamics of the ripple instability onto that direction. However, the study by Devauchelle et. al. [17], which includes oblique perturbations as well as a fixed lid boundary condition, reports that the film is stable for perturbations that are near-perpendicular to the flow direction. This disagreement between our findings and [17] stems from the differences between the respective mechanisms of bed-form stabilization within the underlying models.

As discussed in the review by Charru et. al. [11], most models of flow over erodible beds introduce two sediment-based mechanisms to add stability to the system: a saturation lag in the bed-load density which imposes a minimum bed-form wavelength; and a gravity effect, where an uneven bed tends to flatten itself diffusively due to grain motion along small-scale bed slopes. Devauchelle et. al. [17] obtain stability at short wavelengths as well as for near-perpendicular perturbations as a result of these two mechanisms. The saturation lag mechanism is supported by experimental [3] and observational evidence [12] in the case of aeolian dunes, but it is not clear how effective it would be for a non-turbulent thin meltwater film where grain saltation would be suppressed. The gravity effect is based on experimental studies of grain incipient motion for flow over an inclined bed, e.g., [18, 26]. This effect is most pronounced when the system is near the threshold Shields stress, and it diminishes as the bed stress becomes large [11]. The strength of the gravity effect is a source of uncertainty since there is no comprehensive study on how it varies with grain properties such as diameter, density, shape and cohesion. The uncertainty is magnified in the case of subglacial sediments for which observational records are sparse and varied.

Our model invokes neither of these sediment-based stabilization mechanisms. Instead, we show the hydrodynamics itself stabilizes short wavelengths through the acceleration-diffusion mechanism outlined in Figure 8(b). The stabilizing feedback arises from resolving the linear time-evolution response of the hydrology to the perturbation. Figure 8(b) shows that the bed stress lags the bed-form when the flow diffusion speed is comparable to the bed-form migration speed. Previous models [29, 59, 13, 17] are unable to reproduce this phase lag because they assume quasi-steady flow, namely that the fluid flow adapts instantaneously to any changes in the bed. Quasi-steady flow is justified by arguing that hydrology operates significantly faster than sediment transport ($\gamma \ll 1$). While the assumption may be true for the mean flow of the film, the separation of time scales is unlikely to hold in the vicinity of the bed. Our results from Figure 4 show that even a three order magnitude difference ($\gamma \sim 10^{-3}$) does not suppress stabilization at wavelengths around 0.1 times the film size.

In a real meltwater film setting, both the hydrology-based mechanism and the sediment-based mechanisms likely contribute to the stability of the system. The latter, however, appear to manifest only in specific regimes such as in the presence of saltating flow or, in case of the gravity effect, when the system is close to the critical Shields threshold [11]. Nevertheless, it is possible that the sediment-based mechanisms stabilize near-perpendicular perturbations in meltwater films and limit the instability to the formation of oblique drainage elements, analogous to the bar instability in [17].

7.2 Canal Initiation on Soft Beds Versus Hard Beds

Walder and Fowler [73] and Ng [52] suggest that efficient drainage systems on soft subglacial sediment beds take the form of canals that are incised into the till. Indeed, canals are commonly observed in the subglacial setting (e.g., Rutford Ice Stream, West Antarctica [41]), but it is unclear which processes

lead to their formation. If thin meltwater films collapse by carving into the ice as a consequence of Walder’s instability [72, 74], Röthlisberger channels [60] will dominate the early evolution of the hydrological system. This study presents an alternate framework which emphasizes the role of till and coupled meltwater flow in the formation of till-incised canals.

Subglacial drainage systems with a dynamic till have been studied previously, but have not focused specifically on the initiation of canals. Ng [52] describes the coupled dynamics of hydrology and till in fully-developed subglacial canals. He presents equilibrium conditions of a till-incised canal system that spans tens of kilometers. At this length scale, canal evolution is dictated by mass fluxes of water and sediment rather than smaller scale features such as bed geometry and vertical flow profiles. Our model provides a complementary approach in the sense that we study meltwater films at the length scale of the film thickness and resolve bed geometry and near-bed flow dynamics. Our analysis yields a channel initiation mechanism that may eventually lead to the formation of long drainage systems discussed by Ng.

Kyrke-Smith and Fowler [43] develop a model to understand the evolution of meltwater films on soft beds, where they include the processes of till erosion and deformation and meltwater generation. Since Walder’s mechanism of film expansion via dissipation is known to make meltwater films unstable, [43] introduce the framework of supporting clasts, developed by Creyts and Schoof [14], to suppress Walder’s instability. The key insight from Creyts and Schoof [14] is that clasts distributed within the till bear the majority of the ice overburden stress, and this stress localization leads to faster closure of the ice, thus adding stability to the film.

While the framework of supporting clasts is well suited to subglacial water systems over hard beds, it is not clear that the framework translates to the soft bed setting, especially given the potential for the erosion and plastic deformation [1, 67, 68] of till. Our study highlights an alternate canal initiation mechanism, where we show that meltwater films grow in an unstable manner by eroding the till beneath, long before they reach flow speeds that are sufficient to carve into the ice. In the regime of slow non-turbulent flow, the ice-water interface is decoupled from the film, and the key dynamics lies exclusively between the mechanical interactions of water and sediment. The morphological instability that stems from these sediment-water interactions initiates the transformation of the film into a canal.

Our study provides an interesting contrast to the condition of stability that arises from the supporting clasts framework of Creyts and Schoof [14]. For hard beds, Creyts and Schoof argue that the largest clast size controls the onset of instability within the meltwater film, since the ice overburden stress localizes over the largest clasts eventually as the film grows. Our study suggests that, for plastic beds, sediment grains with the smallest size control the onset of instability, since they are the easiest to erode. While our study does not directly account for multiple grain sizes, work by [48] suggests the possibility that film flow can channelize by preferentially eroding smaller sized grains. Our work thus brings to light a key physical difference between hard and soft beds,

where the smallest grain size controls stability for soft beds, unlike in the hard bed case where stability is controlled by the largest clast size.

8 Conclusion

The linearized stability analysis we have performed in this paper highlights that water transport over soft beds is associated with dynamic bedform evolution in the subglacial till and elucidates the conditions under which evenly spaced canals eroded in the sediment can emerge out of a flat bed as a result of a morphological instability. Our theory for canal initiation would be testable against idealized laboratory experiments of thin film flow over granular beds in a Hele-Shaw cell, which, to our knowledge, are not currently available. The fastest growing wavelength we identify, however, is unlikely to be compatible with subglacial morphologies observed in the field [19]. Our study is limited to the physical processes leading to the initiation of bedforms; making a direct link to field observables would require follow-up work that captures the non-linear evolution of the incipient bedform into its fully-fledged form, for example through a depth-resolved, direct numerical simulation. This would also shed light on whether and how evenly-spaced incipient canals saturate into a network of fully evolved drainage elements that can be analyzed in isolation [73, 52, 53] and perhaps represented in a parametrized form in large-scale hydrological models akin to existing formulations for hard-rock beds [61, 62, 35, 34, 76].

References

- [1] R. Alley, D. Blankenship, C. Bentley, and S. Rooney. Till beneath ice stream b: 3. till deformation: evidence and implications. *Journal of Geophysical Research: Solid Earth*, 92(B9):8921–8929, 1987.
- [2] R. B. Alley. Water-pressure coupling of sliding and bed deformation: I. water system. *Journal of Glaciology*, 35(119):108–118, 1989.
- [3] B. Andreotti, P. Claudin, and O. Pouliquen. Measurements of the aeolian sand transport saturation length. *Geomorphology*, 123(3):343–348, November 2010.
- [4] R. Bagnold. The nature of saltation and of ‘bed-load’ transport in water. *Proceedings of the Royal Society of London A: Mathematical, Physical and Engineering Sciences*, 332(1591):473–504, 1973.
- [5] R. Betchov and W. O. Jr. Criminale. *Stability of Parallel Flows*. Academic Press. New York/London., 1967.
- [6] D. Blankenship, R. Bentley, S. T. Rooney, and R. B. Alley. Seismic measurements reveal a saturated porous layer beneath an active antarctic ice stream. *Nature*, 322(6074):54–57, July 1986.

- [7] Marion Bougamont, Slawek Tulaczyk, and Ian Joughin. Response of subglacial sediments to basal freeze-on 2. application in numerical modeling of the recent stoppage of ice stream c, west antarctica. *Journal of Geophysical Research: Solid Earth*, 108(B4), 2003.
- [8] C. Camporeale, C. Canuto, and L. Ridolfi. A spectral approach for the stability analysis of turbulent open-channel flows over granular beds. *Theoretical and Computational Fluid Dynamics*, 26(1):51–80, Jan 2012.
- [9] C. Camporeale, E. Mantelli, and C. Manes. Interplay among unstable modes in films over permeable walls. *Journal of Fluid Mechanics*, 719:527550, 2013.
- [10] F. Charru, H. Mpuilleron, and O. Eiff. Erosion and deposition of particles on a bed sheared by a viscous flow. *Journal of Fluid Mechanics*, 519:55–80, 2004.
- [11] Francois Charru, Bruno Andreotti, and Philippe Claudin. Sand ripples and dunes. *Annu. Rev. Fluid Mech.*, 45(1):469–493, January 2013.
- [12] P. Claudin, G. F. S. Wiggs, and B. Andreotti. Field evidence for the upwind velocity shift at the crest of low dunes. *Boundary-Layer Meteorology*, 148(1):195–206, July 2013.
- [13] M. Colombini. Revisiting the linear theory of sand dune formation. *Journal of Fluid Mechanics*, 502:1–16, 2004.
- [14] Timothy T. Creyts and Christian G. Schoof. Drainage through subglacial water sheets. *Journal of Geophysical Research: Earth Surface*, 114(F4):F04008, 2009.
- [15] Kurt M Cuffey and Paterson W. S. B. *The physics of glaciers*. Butterworth-Heinemann/Elsevier, Amsterdam [etc.], 2012.
- [16] Anders Damsgaard, Jenny Suckale, Jan A. Piotrowski, Morgane Housais, Matthew R. Siegfried, and Helen A. Fricker. Sediment behavior controls equilibrium width of subglacial channels. *Journal of Glaciology*, 63(242):1034–1048, 2017.
- [17] O. Devauchelle, L. Malverti, . Lajeunesse, P.Y. Lagree, C. Josserand, and K. D. Nguyen. Thu-Lam. Stability of bedforms in laminar flows with free surface: from bars to ripples. *Journal of Fluid Mechanics*, 642:329–348, 2010.
- [18] Subhasish Dey. Threshold of sediment motion on combined transverse and longitudinal sloping beds. *Journal of Hydraulic Research*, 41(4):405–415, July 2003.
- [19] J. A. Dowdeswell, M. Canals, M. Jakobsson, B. J. Todd, E. K. Dowdeswell, and K. A. Hogan. Introduction: an atlas of submarine glacial landforms. *Geological Society, London, Memoirs*, 46(1):3, January 2016.

- [20] P. G. Drazin and W. H. Reid. *Hydrodynamic Stability*. Cambridge Mathematical Library. Cambridge University Press, 2 edition, 2004.
- [21] David J. Drewry. *Antarctica : glaciological and geophysical folio*. Polar Research Institute, Cambridge, Eng., 1983.
- [22] Hans Albert Einstein. *The bed-load function for sediment transportation in open channel flows*, volume 1026. US Department of Agriculture Washington, DC, 1950.
- [23] Cooper W Elsworth and Jenny Suckale. Rapid ice flow rearrangement induced by subglacial drainage in west antarctica. *Geophysical Research Letters*, 43(22):11,697–11,707, 2016.
- [24] Hermann Engelhardt and Barclay Kamb. Basal hydraulic system of a west antarctic ice stream: constraints from borehole observations. *Journal of Glaciology*, 43(144):207–230, 1997.
- [25] D. Evans, E. Phillips, J. Hiemstra, and C. Auton. Subglacial till: formation, sedimentary characteristics and classification. *Earth-Science Reviews*, 78(1-2):115–176, 2006.
- [26] R. Fernandez Luque and R. Van Beek. Erosion and transport of bed-load sediment. *Journal of Hydraulic Research*, 14(2):127–144, April 1976.
- [27] Gwenn E. Flowers. Modelling water flow under glaciers and ice sheets. *Proceedings of the Royal Society of London A: Mathematical, Physical and Engineering Sciences*, 471(2176), 2015.
- [28] J. R. D. Francis. Experiments on the motion of solitary grains along the bed of a water-stream. *Proceedings of the Royal Society of London A: Mathematical, Physical and Engineering Sciences*, 332(1591):443–471, 1973.
- [29] Jorgen Fredsoe. On the development of dunes in erodible channels. *Journal of Fluid Mechanics*, 64(1):1–16, 1974.
- [30] D. V. Georgievskii. Applicability of the squire transformation in linearized problems on shear stability. *Russian Journal of Mathematical Physics*, 16(4):478, Dec 2009.
- [31] Basil Gomez and Michael Church. An assessment of bed load sediment transport formulae for gravel bed rivers. *Water Resources Research*, 25(6):1161–1186, 1989.
- [32] Bernard Hallet. The effect of subglacial chemical processes on glacier sliding. *Journal of Glaciology*, 17(76):209–221, 1976.
- [33] Bernard Hallet. Subglacial regelation water film. *Journal of Glaciology*, 23(89):321–334, 1979.

- [34] I. J. Hewitt. Seasonal changes in ice sheet motion due to melt water lubrication. *Earth and Planetary Science Letters*, 371:16–25, 2013.
- [35] I. J. Hewitt, C. Schoof, and M. A. Werder. Flotation and free surface flow in a model for subglacial drainage. part 2. channel flow. *Journal of Fluid Mechanics*, 702:157–187, 2012.
- [36] Morgane Houssais, Carlos P. Ortiz, Douglas J. Durian, and Douglas J. Jerolmack. Onset of sediment transport is a continuous transition driven by fluid shear and granular creep. *Nature Communications*, 6(6527), March 2015.
- [37] Neal R. Iverson, Robert W Baker, and Thomas S. Hooyer. A ring-shear device for the study of till deformation: tests on tills with contrasting clay contents. *Quaternary Science Reviews*, 16(9):1057–1066, 1997.
- [38] Neal R. Iverson, Thomas S. Hooyer, and Robert W. Baker. Ring-shear studies of till deformation: Coulomb-plastic behavior and distributed strain in glacier beds. *Journal of Glaciology*, 44(148):634–642, 1998.
- [39] John F. Kennedy. The mechanics of dunes and antidunes in erodible-bed channels. *Journal of Fluid Mechanics*, 16(4):521–544, 1963.
- [40] John F. Kennedy. The formation of sediment ripples, dunes, and antidunes. *Annual review of fluid mechanics*, 1(1):147–168, 1969.
- [41] Edward C King, John Woodward, and Andrew M Smith. Seismic evidence for a water-filled canal in deforming till beneath rutford ice stream, west antarctica. *Geophysical Research Letters*, 31(20):L20401, 2004.
- [42] N. P. Kirchner. Computational aspects of the spectral galerkin fem for the orr–sommerfeld equation. *International journal for numerical methods in fluids*, 32(1):105–121, 2000.
- [43] M. Kyrke-Smith T. and C. Fowler A. Subglacial swamps. *Proceedings of the Royal Society A: Mathematical, Physical and Engineering Sciences*, 470(2171):20140340, November 2014.
- [44] M. Kyrke-Smith T., F. Katz R., and C. Fowler A. Subglacial hydrology and the formation of ice streams. *Proceedings of the Royal Society A: Mathematical, Physical and Engineering Sciences*, 470(2161):20130494, January 2014.
- [45] AM Le Brocq, AJ Payne, MJ Siegert, and RB Alley. A subglacial water-flow model for west antarctica. *Journal of Glaciology*, 55(193):879–888, 2009.
- [46] Craig S Lingle and Timothy J Brown. A subglacial aquifer bed model and water pressure dependent basal sliding relationship for a west antarctic ice stream. In *Dynamics of the West Antarctic ice sheet*, pages 249–285. Springer, 1987.

- [47] P Luchini and F Charru. The phase lead of shear stress in shallow-water flow over a perturbed bottom. *Journal of Fluid Mechanics*, 665:516–539, 2010.
- [48] A. Mahadevan, A. V. Orpe, A. Kudrolli, and L. Mahadevan. Flow-induced channelization in a porous medium. *EPL (Europhysics Letters)*, 98(5):58003, 2012.
- [49] Yasmina M. Martos, Manuel Cataln, Tom A. Jordan, Alexander Golynsky, Dmitry Golynsky, Graeme Eagles, and David G. Vaughan. Heat flux distribution of antarctica unveiled. *Geophys. Res. Lett.*, 44(22):11,417–11,426, November 2017.
- [50] Eugen Meyer-Peter and R. Müller. Formulas for bed-load transport. In *IAHSR 2nd meeting, Stockholm, appendix 2*. IAHR, 1948.
- [51] MC Miller, IN McCave, and P_D Komar. Threshold of sediment motion under unidirectional currents. *Sedimentology*, 24(4):507–527, 1977.
- [52] Felix S Ng. Canals under sediment-based ice sheets. *Annals of Glaciology*, 30:146–152, 2000.
- [53] Felix S. Ng. Coupled ice–till deformation near subglacial channels and cavities. *Journal of Glaciology*, 46(155):580–598, 2000.
- [54] Steven A. Orszag. Accurate solution of the orrsommerfeld stability equation. *Journal of Fluid Mechanics*, 50(4):689703, 1971.
- [55] Malika Ouriemi, Pascale Aussillous, Marc Medale, Yannick Peysson, and Élisabeth Guazzelli. Determination of the critical shields number for particle erosion in laminar flow. *Physics of Fluids*, 19(6):061706, 2007.
- [56] Frank Pattyn. Antarctic subglacial conditions inferred from a hybrid ice sheet/ice stream model. *Earth and Planetary Science Letters*, 295(3-4):451–461, 2010.
- [57] Thibaut Perol, James R Rice, John D Platt, and Jenny Suckale. Subglacial hydrology and ice stream margin locations. *Journal of Geophysical Research: Earth Surface*, 120(7):1352–1368, 2015.
- [58] John C Priscu, Slawek Tulaczyk, Michael Studinger, MC Kennicutt, Brent C Christner, and Christine M Foreman. Antarctic subglacial water: origin, evolution and ecology. *Polar lakes and rivers: limnology of Arctic and Antarctic aquatic ecosystems*. Oxford University Press, Oxford, pages 119–135, 2008.
- [59] Kelvin J Richards. The formation of ripples and dunes on an erodible bed. *Journal of Fluid Mechanics*, 99(3):597–618, 1980.
- [60] Hans Röthlisberger. Water pressure in intra-and subglacial channels. *Journal of Glaciology*, 11(62):177–203, 1972.

- [61] Christian Schoof. Ice-sheet acceleration driven by melt supply variability. *Nature*, 468(7325):803–806, 2010.
- [62] Christian Schoof, Ian J Hewitt, and Mauro A Werder. Flotation and free surface flow in a model for subglacial drainage. part 1. distributed drainage. *Journal of Fluid Mechanics*, 702:126–156, 2012.
- [63] Jie Shen. Efficient spectral-galerkin method i. direct solvers of second- and fourth-order equations using legendre polynomials. *SIAM Journal on Scientific Computing*, 15(6):1489–1505, 1994.
- [64] Albert Shields. Anwendung der aehnlichkeitsmechanik und der turbulenzforschung auf die geschiebebewegung. *PhD Thesis Technical University Berlin*, 1936.
- [65] EM Shoemaker. Subglacial hydrology for an ice sheet resting on a deformable aquifer. *Journal of Glaciology*, 32(110):20–30, 1986.
- [66] Slawek Tulaczyk, Barclay Kamb, and Hermann F Engelhardt. Estimates of effective stress beneath a modern west antarctic ice stream from till preconsolidation and void ratio. *Boreas*, 30(2):101–114, 2001.
- [67] Slawek Tulaczyk, Barclay Kamb, Reed P Scherer, and Hermann F Engelhardt. Sedimentary processes at the base of a west antarctic ice stream; constraints from textural and compositional properties of subglacial debris. *Journal of Sedimentary Research*, 68(3):487–496, 1998.
- [68] Slawek Tulaczyk, W Barclay Kamb, and Hermann F Engelhardt. Basal mechanics of ice stream b, west antarctica: 1. till mechanics. *Journal of Geophysical Research: Solid Earth*, 105(B1):463–481, 2000.
- [69] Slawek Tulaczyk, W Barclay Kamb, and Hermann F Engelhardt. Basal mechanics of ice stream b, west antarctica: 2. undrained plastic bed model. *Journal of Geophysical Research: Solid Earth*, 105(B1):463–481, 2000.
- [70] van Rijn Leo C. Sediment transport, part i: Bed load transport. *Journal of Hydraulic Engineering*, 110(10):1431–1456, October 1984.
- [71] Robert Vivian. The nature of the ice-rock interface: The results of investigation on 20000m² of the rock bed of temperate glaciers. *Journal of Glaciology*, 25(92):267–277, 1980.
- [72] Joseph S Walder. Stability of sheet flow of water beneath temperate glaciers and implications for glacier surging. *Journal of Glaciology*, 28(99):273–293, 1982.
- [73] Joseph S Walder and Andrew Fowler. Channelized subglacial drainage over a deformable bed. *Journal of Glaciology*, 40(134):3–15, 1994.
- [74] J Weertman and GE Birchfield. Subglacial water flow under ice streams and west antarctic ice-sheet stability. *Annals of glaciology*, 3:316–320, 1982.

- [75] Johannes Weertman. General theory of water flow at the base of a glacier or ice sheet. *Reviews of Geophysics*, 10(1):287–333, 1972.
- [76] Mauro A. Werder, Ian J. Hewitt, Christian G. Schoof, and Gwenn E. Flowers. Modeling channelized and distributed subglacial drainage in two dimensions. *Journal of Geophysical Research: Earth Surface*, 118(4):2140–2158, 2013.
- [77] M. S. Yalin. *Mechanics of sediment transport*. Pergamon Press Oxford, New York, [1st ed.] edition, 1972.

Supplementary Material: Subglacial Canal Initiation Driven by Till Erosion

Indraneel Kasmalkar, Elisa Mantelli, Jenny Suckale

1 Linearization of the Exner Equation

We introduce the perturbation $\exp(ik_1x + ik_2y + \omega t)$ into the non-dimensional Exner equation (3.3) from the manuscript. Omitting the star notation for non-dimensional variables,

$$\omega r' = -ik_1q'_x - ik_2q'_y, \quad \mathbf{q}' = F(S|\bar{\boldsymbol{\tau}}|)\hat{\boldsymbol{\tau}}' + S|\boldsymbol{\tau}'|dF(S|\bar{\boldsymbol{\tau}}|)\bar{\boldsymbol{\tau}}. \quad (\text{S.1})$$

The non-dimensional bed stress $\boldsymbol{\tau} = (\tau_x, \tau_y)$ and unit bed stress vectors are given by (2.8),

$$\tau_i = \mathbf{t}_i^T (\nabla \mathbf{u} + \nabla \mathbf{u}^T) \mathbf{n}, \quad \hat{\boldsymbol{\tau}} = \frac{\boldsymbol{\tau}}{|\boldsymbol{\tau}|}, \quad \text{at } z = r. \quad (\text{S.2})$$

The vectors $\mathbf{t}_x, \mathbf{t}_y$ are the unit tangent vectors to the bed in the x - and y - directions respectively, and \mathbf{n} is the normal surface vector for the bed $z = r(x, y, t)$,

$$\mathbf{t}_x = \frac{(1, 0, \frac{\partial r}{\partial x})}{\sqrt{1 + (\frac{\partial r}{\partial x})^2}}, \quad \mathbf{t}_y = \frac{(1, 0, \frac{\partial r}{\partial y})}{\sqrt{1 + (\frac{\partial r}{\partial y})^2}}, \quad \mathbf{n} = \frac{(-\frac{\partial r}{\partial x}, -\frac{\partial r}{\partial y}, 1)}{\sqrt{1 + (\frac{\partial r}{\partial x})^2 + (\frac{\partial r}{\partial y})^2}}. \quad (\text{S.3})$$

After introducing the perturbations, these vectors take the form,

$$\mathbf{t}_x = (1, 0, 0) + \varepsilon ik_1 r' (0, 0, 1), \quad \mathbf{t}_y = (1, 0, 0) + \varepsilon ik_2 r' (0, 0, 1), \quad \mathbf{n} = (0, 0, 1) + \varepsilon (ik_1 r', ik_2 r', 0). \quad (\text{S.4})$$

We evaluate the non-dimensional stress terms and their perturbations,

$$\bar{\boldsymbol{\tau}} = (1, 0), \quad \boldsymbol{\tau}' = (Du' + ik_1 w', Dv' + ik_2 w'), \quad \bar{\hat{\boldsymbol{\tau}}} = (1, 0), \quad \hat{\boldsymbol{\tau}}' = (0, Dv' + ik_2 w'). \quad (\text{S.5})$$

Care needs to be taken for the computation for $\hat{\boldsymbol{\tau}}' = \left(\frac{\boldsymbol{\tau}'}{|\boldsymbol{\tau}'|}\right)'$. The perturbation of $|\boldsymbol{\tau}'|$ is given by $|\boldsymbol{\tau}'| = 1 + \varepsilon \text{Real}(Du' + ik_1 w')$.

Thus,

$$\mathbf{q}' = ([Du' + ik_1 w'] S dF(S), F(S) [Dv' + ik_2 w']), \quad (\text{S.6})$$

which yields the linearized Exner equation (5.10),

$$\omega r' = -ik_1 S k dF [Du' + ik_1 w'] - ik_2 \kappa F [Dv' + ik_2 w']. \quad (\text{S.7})$$

2 Numerics

For reference, we write the main system of equations (5.20 - 5.23) from the manuscript,

$$\gamma \omega [D^2 - k^2] \psi = -ik_1 [\bar{u} D^2 \psi - \psi D^2 \bar{u} - k^2 \bar{u} \psi] + \frac{1}{\text{Re}} [D^2 - k^2]^2 \psi, \quad (\text{S.7})$$

$$D\psi = 0, \quad \psi = 0, \quad \text{at } z = 2, \quad (\text{S.8})$$

$$D\psi = -\sin(\theta) L D \bar{u} r', \quad \psi = 0, \quad \text{at } z = 0, \quad (\text{S.9})$$

$$\omega r' = -ik \kappa F D^2 \psi \quad \text{at } z = 0, \quad (\text{S.10})$$

where $\psi(z)$ is the streamfunction, z corresponds to the coordinate along the film depth, Re is the Reynolds number, $\bar{u}(z)$ is the steady state velocity along the x -direction, r' is the bed-form perturbation amplitude, k is the perturbation wavenumber, F is the steady state non-dimensional bed-load flux value, θ is the Squire angle, $k_1 = k \sin \theta$ and κ is a non-dimensional variable that connects the model scaling to that of the standard bedload transport scaling. We present the details of spectral Galerkin solver for the equations (S.7 - S.10). For the purpose of the solver, we perform the translation $\zeta = z - 1$. We define the modified Sobolev space,

$$H_{\pm 1}^2[-1, 1] = \left\{ \varphi \in L^2[-1, 1] : \varphi(\pm 1) = 0, \frac{d\varphi}{d\zeta}(\pm 1) = 0, \frac{d^j \varphi}{d\zeta^j} \in L^2[-1, 1], \quad 0 \leq j \leq 2 \right\}, \quad (\text{S.12})$$

where $L^2[-1, 1]$ is the space of all square-integrable functions on $-1 \leq \zeta \leq 1$.

We write (S.7) in weak form by integrating against $\varphi \in H_1^2[-1, 1]$,

$$\omega M(\psi, \varphi) = A(\psi, \varphi), \quad (\text{S.13})$$

where $M(\psi, \phi)$ and $A(\psi, \phi)$ are the mass and the stiffness bilinear forms, respectively,

$$M = \gamma [I_{20} - k^2 I_{00}], \quad A = ik_1 [U_{200} - U_{020} + k^2 U_{000}] + \frac{1}{Re} [I_{22} - 2k^2 I_{20} + k^4 I_{00}], \quad (\text{S.14})$$

$$\text{and, } I_{j_1 j_2}(\psi, \varphi) = \int_{-1}^1 \frac{d^{j_1} \psi}{d\zeta^{j_1}} \frac{d^{j_2} \varphi}{d\zeta^{j_2}} d\zeta, \quad U_{j_1 j_2 j_3}(\psi, \varphi) = \int_{-1}^1 \frac{d^{j_1} \bar{u}}{d\zeta^{j_1}} \frac{d^{j_2} \psi}{d\zeta^{j_2}} \frac{d^{j_3} \varphi}{d\zeta^{j_3}} d\zeta. \quad (\text{S.15})$$

In (S.14) we use integration by parts, combined with boundary terms equaling zero due to (S.12).

We approximate the solution space for ψ by the finite dimensional subspace,

$$V_N = \text{Span}\{\psi_j : -1 \leq j \leq N\}, \quad (\text{S.16})$$

where, for $1 \leq j \leq N$, we define ψ_j as the double-integrated Legendre polynomial L_{j+1} such that $\psi_j(\pm 1) = \frac{d\psi_j}{d\zeta}(\pm 1) = 0$, namely,

$$\psi_j = \sqrt{j + \frac{3}{2}} \left(\frac{L_{j+3} - L_{j+1}}{(2j+3)(2j+5)} - \frac{L_{j+1} - L_{j-1}}{(2j+1)(2j+3)} \right), \quad (\text{S.17})$$

and ψ_0, ψ_1 correspond to two low-degree polynomials, linearly independent from the other ψ_j , to incorporate the two boundary conditions (S.9) at the till-water interface,

$$\psi_0(z) = (\zeta - 1)^2, \quad \psi_{-1}(z) = (\zeta - 1)^2(\zeta + 2). \quad (\text{S.18})$$

We write the solution as $\psi = \sum_{j=-1}^N a_j \psi_j$. Note that the ice-water boundary conditions (S.8) would be automatically satisfied by any such ψ . We incorporate the boundary conditions (S.9) and the Exner equation (S.10) in strong form.

We approximate the test function space $H_{\pm 1}^2[-1, 1]$ by the finite dimensional subspace W_N , which consists of just the standard basis functions without the low-degree polynomials.

$$W_N = \text{Span}\{\psi_j : 1 \leq j \leq N\}. \quad (\text{S.19})$$

We reformulate the bilinear forms A, I, U and M in (S.13) as $(N+3) \times (N+3)$ matrices. The $N+3$ columns stand the unknowns represented by $\mathbf{x} = (a_{-1}, a_0, a_1, \dots, a_N, r')$. The $N+3$ rows stand for integration against the N test functions of W_N , plus three additional rows that describe the two boundary conditions (S.9) and the Exner equation (S.10). With we obtain a finite dimensional eigenvalue problem, $A\mathbf{x} = \omega M\mathbf{x}$, which we solve using the Matlab *eig* routine.

3 Asymptotic Analysis

3.1 Short Wavelength Diffusion

The analytical solution of the reduced model (6.7 - 6.10) for the short wavelength diffusion-only regime is given by,

$$\psi^{(0)} = -2z^{(0)} \exp(-z^{(0)}), \quad \omega^{(0)} = -4i, \quad (\text{S.20})$$

We compare the theoretical value of ω , given above, and the rescaled numerical results, $\omega_{\text{num}} = \frac{\omega}{FLk^2 \sin \theta}$ in Figure S1. The figure shows good agreement between the numerical and theoretical solutions.

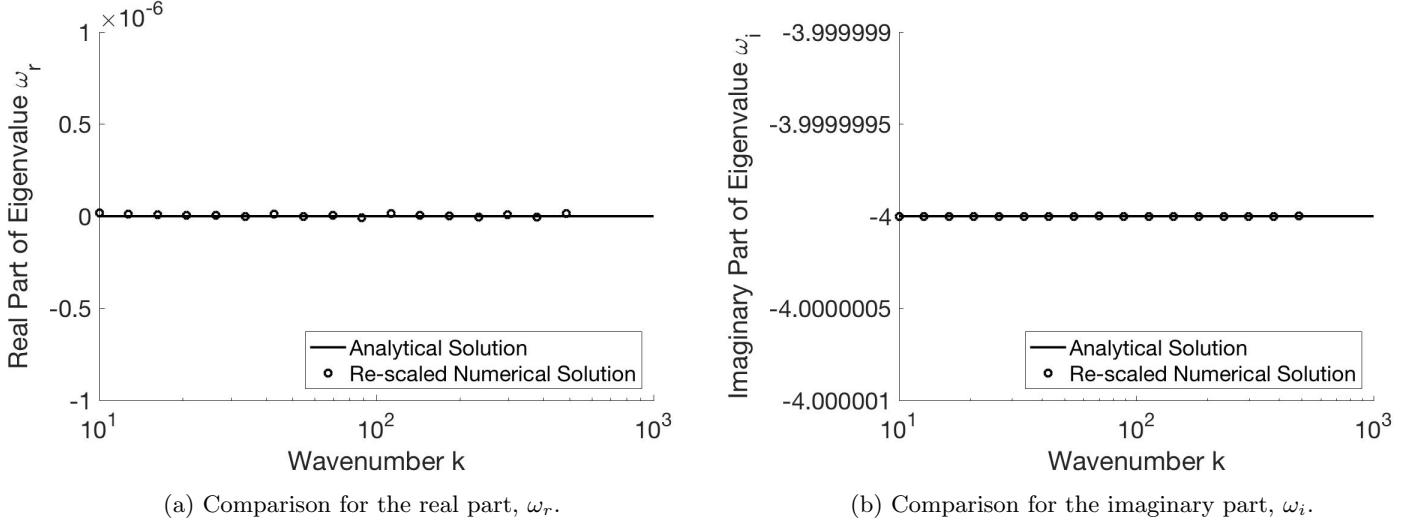


Figure S1: Analytical and re-scaled numerical solutions for the short wavelength diffusion regime.

3.2 Long Wavelength Diffusion

The analytical solution of the reduced model (6.16 - 6.19) for the long wavelength diffusion-only regime is given by,

$$\psi = -2z + 2z^2 - 0.5z^3, \quad \omega = -4i, \quad (\text{S.21})$$

We compare the theoretical value of ω , given above, and the rescaled numerical results, $\omega_{\text{num}} = \frac{\omega}{FLk \sin \theta}$. Figure S2 suggests that the numerical result converges to the theoretical value as $k \rightarrow 0$.

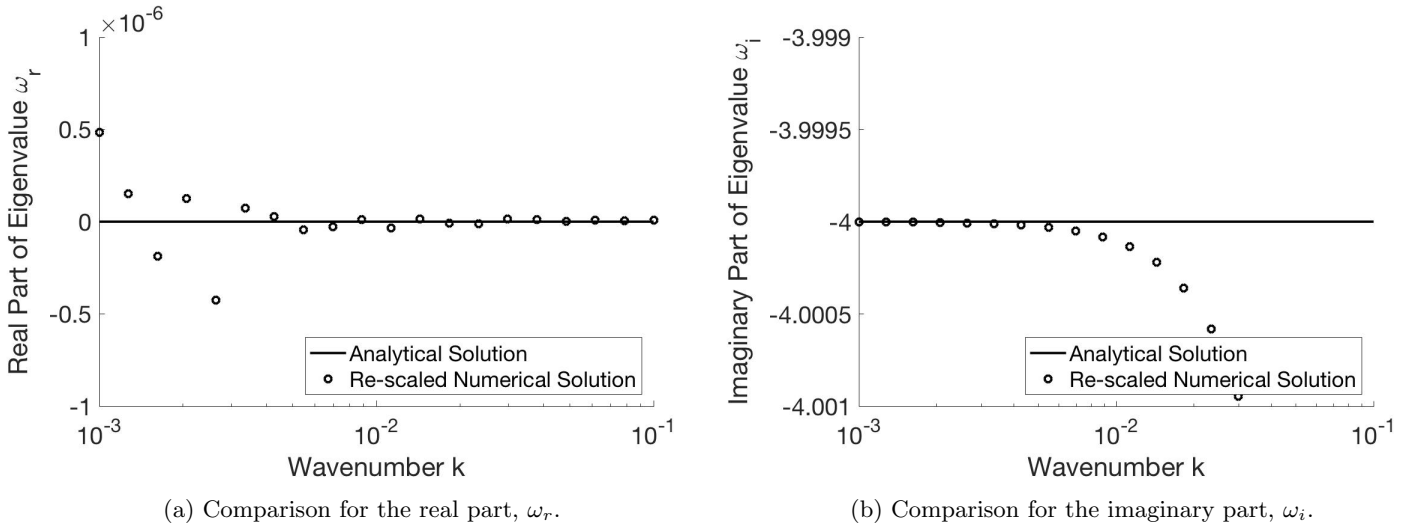


Figure S2: Analytical and re-scaled numerical solutions for the long wavelength diffusion regime. (a) exhibits ill-conditioning as $k \rightarrow 0$.

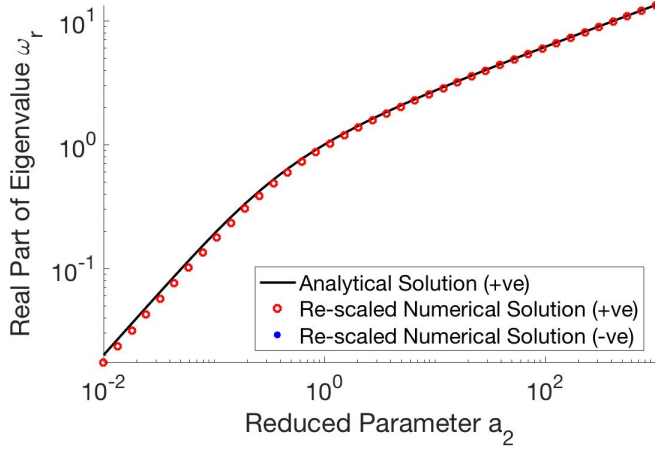
3.3 Short Wavelength Advection

The analytical solution of the reduced model (6.21, 6.8 - 6.10) for the short wavelength advection-diffusion regime is given by,

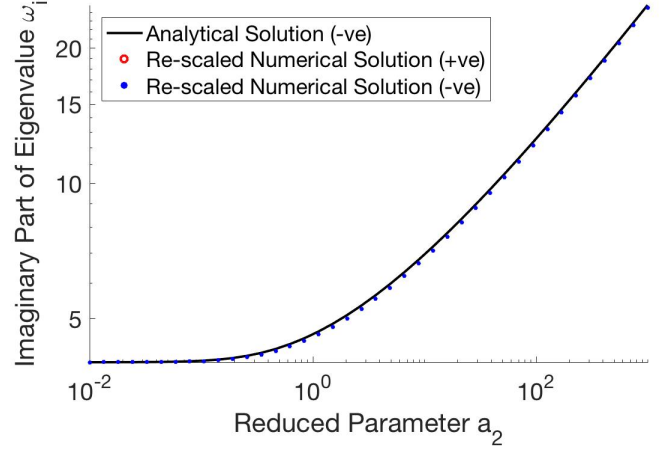
$$\psi = \frac{2 \int_0^z \int_v^\infty e^{2v-s-z} \text{Ai}(c^{-1}s + c^2) ds dv}{\int_0^\infty e^{-s} \text{Ai}(c^{-1}s + c^2) ds}, \quad \omega = \frac{-2i \text{Ai}(c^2)}{\int_0^\infty e^{-s} \text{Ai}(c^{-1}s + c^2) ds}, \quad (\text{S.22})$$

where $c = \frac{1}{\sqrt[3]{2ia_2}}$ with $\arg(c) = -\frac{\pi}{6}$, and $\text{Ai}(z)$ is one of the two standard linearly independent solutions of the system $D^2 f = zf$. The integrals in (S.22) converge due to the exponential decay rate of $\text{Ai}(z)$ for $-\frac{\pi}{3} < z < \frac{\pi}{3}$.

We compare the theoretical value of ω , given above, and the rescaled numerical results, $\omega_{\text{num}} = \frac{\omega}{FLk^2 \sin \theta}$ in Figure S3.



(a) Comparison for the real part, ω_r .



(b) Comparison for the imaginary part, ω_i .

Figure S3: Analytical and re-scaled numerical solutions for the short wavelength advection regime.

3.4 Long Wavelength Advection

We reduce the re-scaled OS equation (6.13) for long wavelengths ,

$$b_1 \omega (D^{*2} - k^2) \psi^* = -ib_2 \left[(2z^* - z^{*2}) (D^{*2} - k^2) + 2 \right] \psi^* + (D^{*2} - 1)^2 \psi^*, \quad (\text{S.23})$$

by $b_1 \rightarrow 0$ to suppress acceleration, and an asymptotic expansion around $k = 0$ for the long wavelength regime,

$$ib_2 \left[z^{(0)} (2 - z^{(0)}) D^2 + 2 \right] \psi^{(0)} = D^4 \psi^{(0)}, \quad b_2 = \text{Re} k \sin \theta. \quad (\text{S.24})$$

We find a semi-analytic solution for (S.24), and the associated boundary conditions for the long wavelength regime (6.17 - 6.19) on $0 \leq z \leq 2$ via a Taylor expansion at $z = 0$. We solve the reduced model for the coefficients of $1, z, z^2, \dots, z^{n-1}$, $n = 12$ using the Matlab symbolic toolbox. We compute $D^2 \psi^{(0)}(0)$ to first order,

$$D^2 \psi^{(0)}(0) = \frac{1436400ib_2^2 + 18711000b_2 - 98232750i}{-14336b_2^5 + 280704ib_2^4 + 2106720b_2^3 + 476280ib_2^2 + 7484400b_2 - 49116375i} + 2. \quad (\text{S.25})$$

We assume $b_2 \ll 1$, which is justified for $\theta \ll 1$. We compute $\omega^{(0)}$ by approximating $D^2 \psi^{(0)}(0)$ with a first-order Taylor expansion at $b_2 = 0$,

$$\omega^{(0)} = D^2 \psi^{(0)}(0) \approx 4 + 0.762ib_2. \quad (\text{S.26})$$

We compare the theoretical value of ω , given above, and the rescaled numerical results, $\omega_{\text{num}} = \frac{\omega}{FLk^2 \sin \theta}$. Figure S4 highlights that the numerical result converges to the theoretical value as $k \rightarrow 0$. For small wavenumbers, the figure also displays ill-conditioning effects.

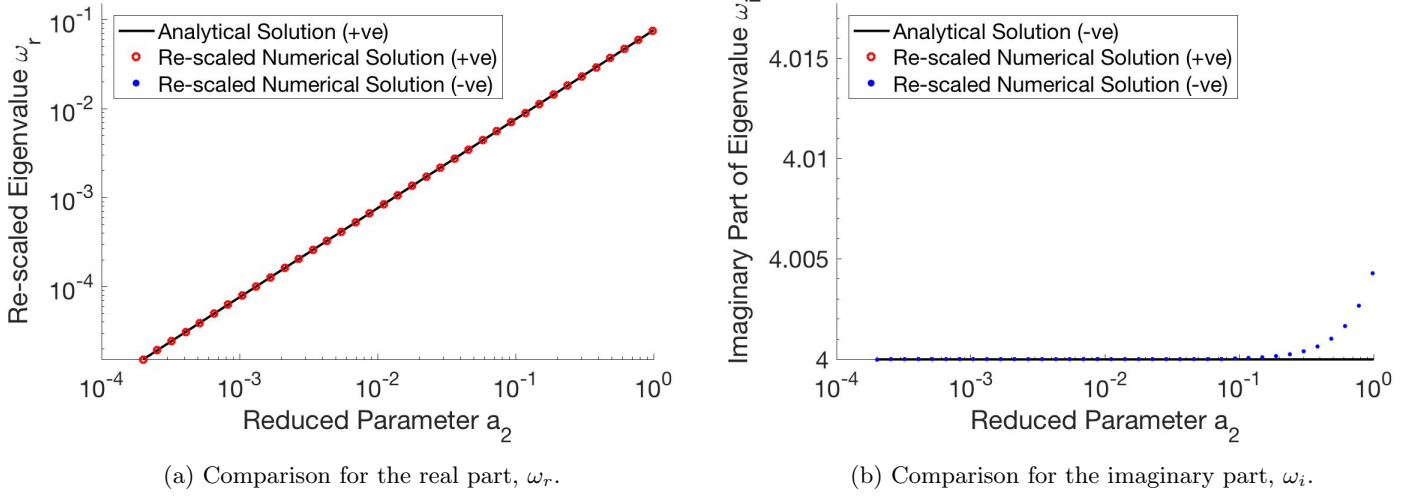


Figure S4: Analytical and re-scaled numerical solutions for the long wavelength advection regime.

3.5 Short Wavelength Acceleration

The analytical solution for the reduced model (6.23, 6.8 - 6.10) is given by,

$$\psi^{(0)} = \frac{2i \left(e^{-z^{(0)}(1-ia_1)} - e^{-z^{(0)}} \right)}{a_1}, \quad \omega^{(0)} = -2a_1 - 4i, \quad (\text{S.27})$$

where $a_1 = FLRe\gamma\kappa \sin \theta$.

We compare the theoretical value of ω , given above, and the rescaled numerical results, $\omega_{\text{num}} = \frac{\omega}{FLk^2 \sin \theta}$ in Figure S5.

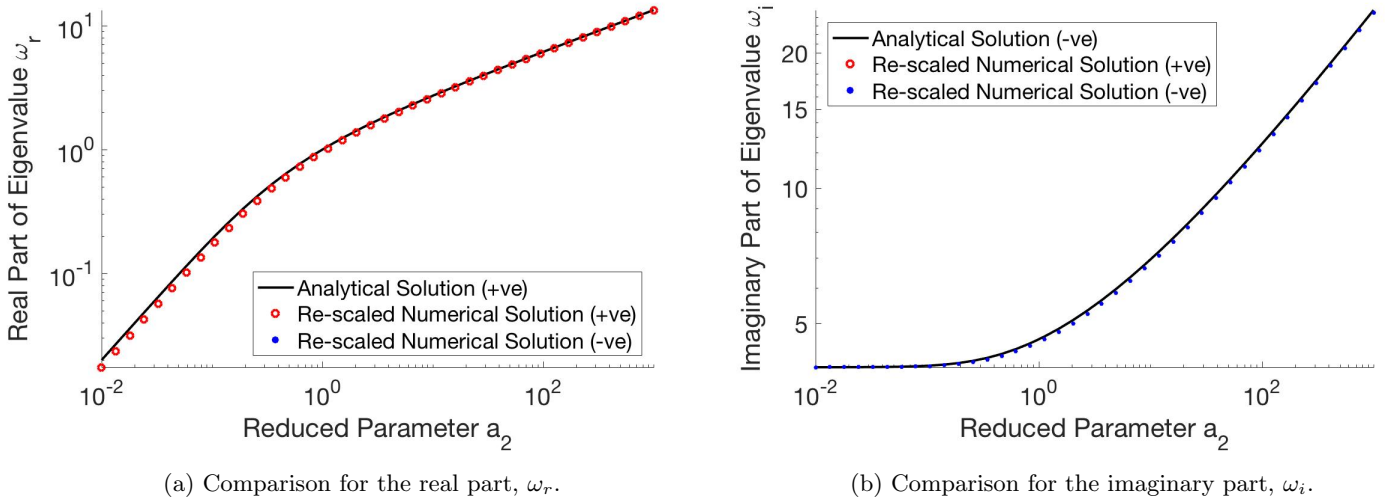


Figure S5: Analytical and re-scaled numerical solutions for the short wavelength advection regime.

3.6 Long Wavelength Acceleration

We reduce the re-scaled OS equation (6.13) for long wavelengths,

$$b_1 \omega (D^{*2} - k^2) \psi^* = -ib_2 \left[(2z^* - z^{*2}) (D^{*2} - k^2) + 2 \right] \psi^* + (D^{*2} - 1)^2 \psi^*, \quad (\text{S.28})$$

by $b_1 \rightarrow 0$ to suppress acceleration, and an asymptotic expansion around $k = 0$ for the long wavelength regime,

$$b_1 \omega^{(0)} D^2 \psi^{(0)} = D^4 \psi^{(0)}. \quad (\text{S.29})$$

This linear ordinary differential equation has characteristic roots, $0, 0, \pm \sqrt{b_1 \omega^{(0)}}$. We use the Matlab symbolic toolbox to solve the above equation. along with associated boundary conditions in the long wavelength regime (6.17 - 6.19), for $0 \leq z \leq 2$. We then symbolically compute $D^2 \psi^{(0)}$ as a function of $\sqrt{b_1 \omega^{(0)}}$. Assuming $b_1 < 1$, which is justified since $L \ll 1$, we perform a second-order Taylor expansion of $D^2 \psi^{(0)}(0)$ around $\sqrt{b_1 \omega^{(0)}} = 0$ to get,

$$D^2 \psi^{(0)}(0) \approx A_0 + A_2 \left(\sqrt{b_1 \omega^{(0)}} \right)^2, \quad A_0 = 3.7584, \quad A_2 = 2.2014. \quad (\text{S.30})$$

The Exner equation yields,

$$\omega^{(0)} = \frac{A_0}{i - A_2 b_1}. \quad (\text{S.31})$$

We compare the theoretical value of ω , given above, and the rescaled numerical results, $\omega_{\text{num}} = \frac{\omega}{FLk \sin \theta}$ in Figure S6.

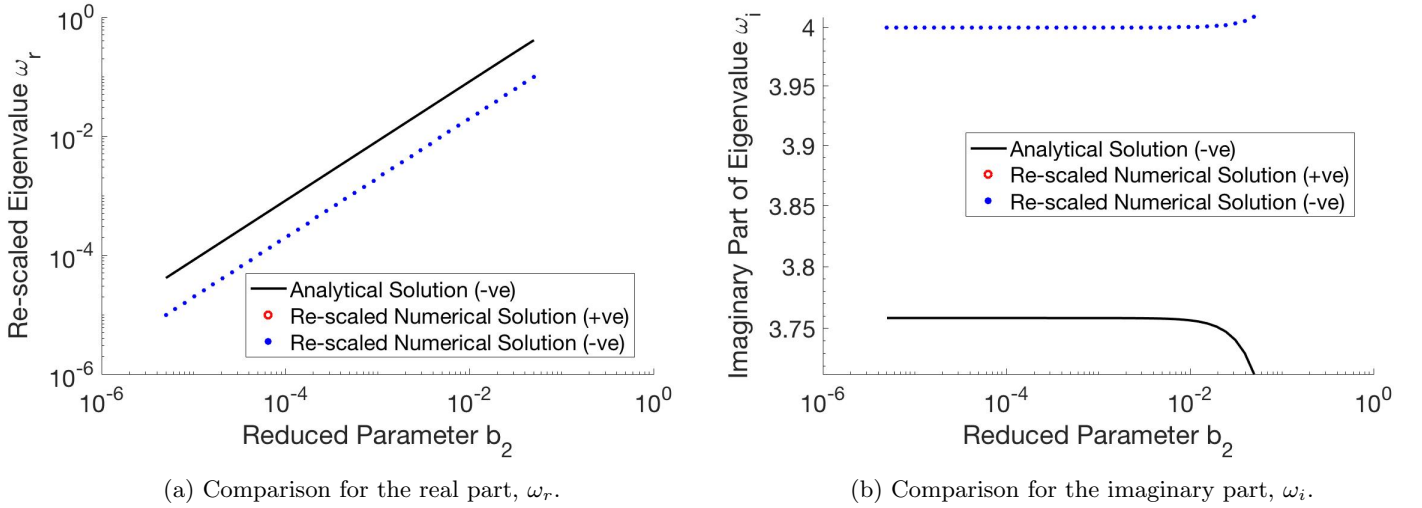


Figure S6: Analytical and re-scaled numerical solutions for the long wavelength acceleration regime.